Modeling and Numerical Implementation of Managed-Pressure-Drilling Systems for the Assessment of Pressure-Control Systems

S. Naderi Lordejani and **M. H. Abbasi,** Eindhoven University of Technology; **N. Velmurugan,** MINES ParisTech; **C. Berg** and **J. Å. Stakvik,** Kelda Drilling Controls; **B. Besselink,** University of Groningen; **L. Iapichino,** Eindhoven University of Technology; **F. Di Meglio,** MINES ParisTech; **W. H. A. Schilders,** Eindhoven University of Technology; and **N. van de Wouw,** Eindhoven University of Technology and University of Minnesota

Summary

Automated managed-pressure drilling (MPD) is a method to enhance downhole pressure-control performance and safety during drilling operations. It is becoming more common to use model-based simulation for the evaluation of pressure-control systems designed for MPD automation before using those in the field. This demands a representative hydraulics-simulation model that captures the relevant aspects of a drilling system. This paper presents such a model and an approach to numerically implement that model for simulation studies. The complexity of this simulation model should be limited, first, to support effective numerical implementation and, second and most importantly, to allow for the analysis of the behavior and performance of the automated pressure-control systems during the controller-design phase. To this end, aspects of a drilling system that can considerably affect the performance of the automated MPD system are captured in the model. This hydraulics model incorporates both the distributed and multiphase-flow nature of a drilling system. Moreover, it captures nonlinear boundary conditions at the inlet of the drillstring, at the drill bit, and choke manifold, and also the variations in the cross-sectional area of the flow path. Model validations against field data from real-life MPD operations and simulations of industry-relevant scenarios indicate that these aspects are effectively captured in the model and preserved during the numerical implementation.

Introduction

Conventionally, the task of pressure control is accomplished by changing the mud density during drilling operations. However, this method of controlling the pressure is slow and inaccurate, and it lacks a means of compensating and responding to transient pressure fluctuations (e.g., occurring during pipe-connection operations or drilling into high-pressure formations). Besides, this method cannot be used for drilling deep wells with narrow drilling windows because of its low accuracy. To overcome such drawbacks of conventional pressure-control methods, MPD has been introduced. A main objective of MPD is to provide a means of fast, accurate, and efficient control of the bottomhole pressure, as opposed to conventional methods. As we illustrate in **Fig. 1,** in MPD, the annulus is sealed off at the top with a rotating control device to direct the mud flow from the annulus to a choke valve with a variable opening (Stamnes et al. 2008; Godhavn 2010). This equipment, which is often accompanied by a backpressure pump, pressurizes the fluid inside the wellbore by providing an active backpressure. The backpressure, and thus the bottomhole pressure, can be controlled by manipulating the choke opening. In automated MPD systems, the task of manipulating the choke opening is primarily performed by an automatic pressure-control system. This enhances safety and performance and reduces drilling time and cost (Godhavn et al. 2011). In particular, if equipped with advanced control systems, automated MPD can make it possible to handle many well-control events automatically without operator intervention and using conventional well-control methods (Berg et al. 2019a).

A control system designed for automated MPD should pass some virtual and representative test scenarios on a simulation level before it can be used in the field. These are performed because any failure in the drilling system, especially in the pressure-control system, can have catastrophic consequences. Training new operators for drilling operations and well-control incidents in a controlled environment, as well as well monitoring, are other important reasons for performing model-based simulation studies in drilling (Cayeux et al. 2012; Vishnumolakala et al. 2015). However, simulations performed for training purposes often need to be well-supported by graphical interfaces, which is not the case when it comes to controller design. These simulations rely on a mathematical model of the drilling-system dynamics, the complexity of which varies depending on the required purpose. In particular, the complexity of an MPD model developed for testing pressure controllers should be limited to facilitate the performance analysis and design of the control system by neglecting less-important system aspects. Such a model, called the simulation model in this context, should only contain aspects of a drilling system considered in the controller designed, and aspects that are not considered in the controller design but can have detrimental effects on the performance of the controller. Models used in the controller design are called the design models. A design model is often much simpler than a simulation model because it usually contains only the mass-transport dynamics, neglecting the distributed nature of drilling systems (Nygaard and Nævdal 2006; Di Meglio et al. 2009; Kaasa et al. 2012; Aarsnes et al. 2016b; Pedersen et al. 2018). The following are a number of the drilling aspects that can be detrimental to an automated MPD system.

- Pressure-wave propagation: Pressure controllers are usually dependent on simplified models in which pressure dynamics (i.e., wave-propagation effects) are ignored partially (Landet et al. 2013) or totally (Stamnes et al. 2008; Di Meglio et al. 2009; Kaasa et al. 2012; Aarsnes et al. 2016b; Ambrus et al. 2016; Nikoofard et al. 2017; Pedersen et al. 2018). The essential time scale associated with these dynamics can be in the range of tens of seconds, or even minutes, in the case of gas influx into the wellbore. Not only can such dynamics deteriorate the control performance, but they can also cause instability (Pedersen et al. 2015), if not accounted for during the controller-design stage.

Original SPE manuscript received for review 30 April 2019. Revised manuscript received for review 9 January 2020. Paper (SPE 201108) peer approved 23 January 2020.

- Dynamics of the flow in the drillstring: In many cases (Aarsnes et al. 2016a), the dynamics of the flow in the drillstring (as opposed to the flow through the annulus), whether fast or slow, are ignored throughout the controller-design stage. This part can, however, have a significant contribution to the system behavior (e.g., by changing the location of the major resonance frequencies of the system or generating additional resonance frequencies). Thus, the closed-loop performance in practice can be worse than expected from simulation studies if system aspects imposed by the drillstring are ignored in the design model.
- Nonlinear behavior of the drill bit: Once the drillstring flow path is ignored in the design model, the drill bit is replaced by an independent source of flow. The flow through the bit is, however, nonlinearly dependent on the pressure drop over the bit. In particular, in the case of standpipe pressure control during gas influxes, this nonlinearity can be detrimental.
- The variable structure (i.e., switching nature) of the model: This variable structure is induced mainly by the presence of a non-return valve in the bottomhole assembly. During operations such as pipe connection, the non-return valve usually remains closed, changing the system properties and behavior.
- Variations in the cross-sectional area of the flow path: These variations, especially those in the annulus, can have significant contributions to the frequency responses of a drilling system. Therefore, if not included in the design model, these aspects can compromise the control performance.

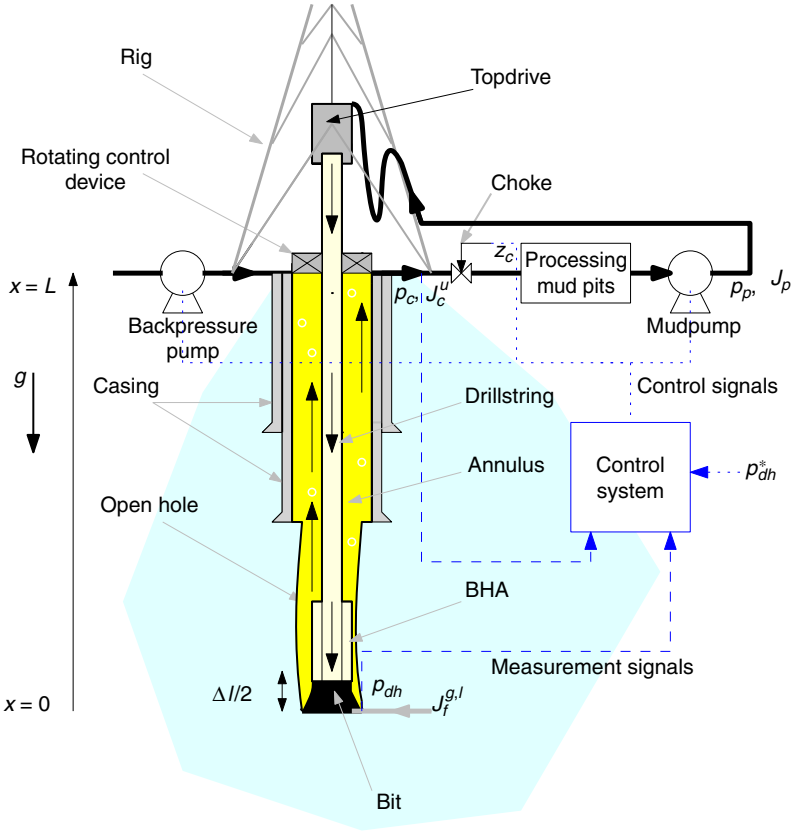

Fig. 1—Simplified schematic of a drilling system with MPD equipment. BHA = bottomhole assembly.

Other dynamical effects, such as temperature transients, evolve so slowly [e.g., see Fig. 14 in Cayeux et al. (2012)] that these can be neglected in the simulation model. These effects can be modeled in terms of uncertainties in the system parameters. Effects such as well expansion can also be approximately lumped into the system parameters (Berg et al. 2019b).

In this paper, we rely on physical simplifications to derive a simulation model for MPD that is consistent with the modeling choices listed previously. The simulation of the resulting model uses a numerical discretization method. Because these numerical methods are incapable of exactly preserving all the characteristics of the model, particular care should be taken in choosing, developing, and using these numerical methods. Thus, we also provide a dedicated numerical approach for the simulation of this model.

The majority of existing hydraulics-simulation models for drilling are single-phase models, often derived from the (isothermal) Euler model (Landet et al. 2012; Naderi Lordejani et al. 2018), and two-phase models, which are often derived from either the two-fluid model or the drift-flux model (DFM) (Lage et al. 2003; Nygaard and Nævdal 2006; Shekari et al. 2013; Udegbunam et al. 2015; Aarsnes et al. 2016d; Strecker et al. 2017; de Carvalho et al. 2019). In MPD modeling, it is key to specify the boundary conditions of the system carefully because exactly these boundary conditions differentiate MPD from conventional drilling methods and are means of applying control inputs. Moreover, one should consider the fact that the flow path in a drilling system, from the rig pump to drill bit all the way up to the choke, experiences discontinuities in its cross-sectional area. These discontinuities have a considerable contribution to the transient- and steady-state behavior of the flow and pressure along the flow path. These issues have not been addressed adequately in the literature. Lage et al. (2003) showed, by means of simulations and experiments on test wells, the predictive capabilities of the DFM for drilling operations. Although they provided an advanced numerical setting for the simulation of their model, they performed their studies in a conventional drilling setting, not MPD. They did also not consider variations in the cross-sectional area of the flow. The work by Wei et al. (2018) is similar to Lage et al. (2003), but the drilling model is solved with a different numerical scheme to improve the solution accuracy. Aarsnes et al. (2016b) used the DFM as a basis for simulating the annulus, testing controllers, and

model-complexity reduction for MPD. The issue of variations in the cross-sectional area was, however, not addressed. A similar hydraulics model was studied in Udegbunam et al. (2015), where only the annulus was considered in the model and an extrapolation method was used for solving the considered boundary conditions for simulations. Shekari et al. (2013) used the two-fluid model for the simulation of the flow in the annulus. Cayeux et al. (2012) provided a survey on advances in drilling simulators, but no technical details were given on the underlying mathematical models. In this paper, we propose a model for two-phase flow MPD drilling operations using the DFM. This model takes all the relevant aspects, mentioned previously, into account.

Contributions. The main contribution of this paper is a simulation platform suitable for evaluating controller performance for MPD operations, which includes both the physical model and the tool to implement it. In particular, a comprehensive formulation of a hydraulics model for MPD-relevant two-phase-flow drilling scenarios is presented first. In this model, interactions between different parts of a drilling system are formulated in terms of boundary conditions. The complexity of the model is limited to contain control-relevant hydraulics aspects of drilling-system dynamics that can in some way be detrimental to the closed-loop performance of an automated MPD. The developed model allows for the simulation of many drilling scenarios ranging from making pipe connections, choke plugging and choke swapping, and bit-nozzle plugging to liquid- and gas-influx scenarios. Then, we provide a numerical approach to support simulation tooling for fast scenario testing. In particular, we adapt a characteristics-based method to solve the nonlinear boundary conditions, and also propose a dynamical model for the drill bit to circumvent numerical issues that appear at low pump-flow rates. Because the effects of variations in the cross-sectional area of the flow path can be significant both on the transient- and steady-state responses of the system, we explicitly address these variations during the numerical implementations of the model. Finally, we validate the hydraulics model for relevant MPD scenarios of single-phase flow by comparing it with a set of field data obtained from commissioning tests of an automated MPD system.

Outline. The next section is devoted to providing a short introduction to the DFM. Next, the mathematical modeling of the system is discussed. The steady-state solution of the model is discussed afterward. After completing the modeling part, we present a numerical approach for the implementation of the model, which is later illustrated by means of a simulation study.

DFM

This section provides a short introduction to the DFM (Gavrilyuk and Fabre 1996) because it is the cornerstone of the MPD model to be developed. Flow behavior in a transmission line can, to some extent, be described by the DFM. Because of its relative simplicity yet favorable capabilities in capturing the pressure and mass-transport dynamics of two-phase flows, the DFM is probably the most widely used model in literature on the control and simulation of two-phase drilling scenarios (Aarsnes et al. 2016d). Consisting of two mass-conservation equations and one combined momentum-conservation equation, the DFM reads as

$$\frac{\partial q}{\partial t}+\frac{\partial f(q)}{\partial x}=S, \quad (1)$$

with

$$q=\begin{bmatrix} q_1\\ q_2\\ q_3\end{bmatrix}:=\begin{bmatrix}\rho_l\alpha_l\\ \rho_g\alpha_g\\ \rho_l\alpha_l v_l+\rho_g\alpha_g v_g\end{bmatrix},\quad f:=\begin{bmatrix}\rho_l\alpha_l v_l\\ \rho_g\alpha_g v_g\\ \rho_l\alpha_l v_l^2+\rho_g\alpha_g v_g^2+p\end{bmatrix},\quad S:=\begin{bmatrix}\Gamma_l\\ -\Gamma_g\\ s(u,t,x)\end{bmatrix}, \quad (2)$$

where $x \in (0, L)$ and $t > 0$ are the spatial and time variables, respectively, with L being the length of the computational domain and the well in this case. The volume fraction, density, velocity, and pressure are denoted by $\alpha=\alpha(t,x)$, $\rho=\rho(t,x)$, $v=v(t,x)$ and $p=p(t,x)$, respectively, where the subscript l denotes the liquid phase and g refers to the gas phase. The vector of primitive variables (individual variables that have a clear physical meaning) is indicated by $u=[\alpha_l,\rho_l,v_l,\alpha_g,\rho_g,v_g,p]^T$, while q represents the vector of conservative variables and $f(\cdot)$ is the flux function. The source term is represented by $s(u,t,x)$, and Γ_l and Γ_g model mass exchange between the phases, which are often assumed to be zero. The source term consisting of a gravitational and frictional term is given by

$$s(u,t,x)=\rho_m g\sin(\theta)-\frac{2\nu(u)\rho_m v_m|v_m|}{D}, \quad (3)$$

where g and $\theta(x)$ are the gravitational acceleration and the inclination of the transmission line with reference to the horizontal direction, and D is the hydraulic diameter. Moreover, $\rho_m=\alpha_l\rho_l+\alpha_g\rho_g$ and $v_m=\alpha_l v_l+\alpha_g v_g$ are the mixture density and velocity, respectively. Here, ν is the Fanning friction factor, which is in general a challenging parameter to determine. It is well-known that drilling muds in general exhibit non-Newtonian behaviors (Reed and Pilehvari 1993). There are a number of models describing these types of flows, such as the Herschel-Bulkley, Bingham plastic, and the power-law model. Of these three, the three-parameter model of Herschel-Bulkley is the most accurate because it includes the other two models as special cases. However, the respective equations are highly nonlinear and challenging to solve and, moreover, complex models with too many parameters are less useful from a control and estimation perspective. Here, we adapt the two-parameter power-law model to trade off between complexity and accuracy. In this model, we define the generalized Reynolds number as $\mathrm{Re}=\rho_m v_m D_{\mathrm{eff}}/\mu_{m,\mathrm{app}}$, where $D_{\mathrm{eff}}=4n_m D/(3n_m+1)$ is the effective diameter and

$$\mu_{m,\mathrm{app}}=\mu_m^{n_m}\left(\frac{3n_m+1}{4n_m}\frac{8v_m}{D}\right)^{n_m-1}, \quad (4)$$

is the apparent mixture viscosity (Reed and Pilehvari 1993). Here, $n_m=\alpha_l n_l+\alpha_g$, with n_l being the liquid-behavior index, is the mixture-behavior index, and $\mu_m=\alpha_l m_l+\alpha_g\mu_g$, with μ_l and μ_g being the liquid and gas viscosity, respectively, is the mixture viscosity. The Fanning friction factor for laminar flow, when $\mathrm{Re}<3,250-1,150n_m$, is given by

$$\nu=\frac{16}{\mathrm{Re}}, \quad (5)$$

while for the turbulent flow, when $\mathrm{Re}>$ 4,250–1,150n_m, ν is the solution to

$$\frac{1}{\sqrt{\nu}}+4\log\left\{\frac{0.27\varepsilon}{D_{\text{eff}}}+\frac{1.26^{n_m^{-1.2}}}{\left[\nu\left(1-\frac{n_m}{2}\right)\text{Re}\right]^{n_m^{-0.75}}}\right\}=0, \quad \ldots\ldots (6)$$

where ε is the pipe roughness (Reed and Pilehvari 1993). As can be seen, Eq. 6 is highly nonlinear and no exact explicit solution is currently available to it; thus, we use an approximate solution (see Appendix A). For transition flow, when $\text{Re}\in[3,250,4,250]-1,150n_m$, we compute ν by a linear interpolation from Eqs. 5 and 6. We stress again that one can use a different frictional model depending on the application and required accuracy; Livescu (2012) provides a review of these models.

Remark 1. The power-law model is in general considered to be complex when it comes to the design of controllers and estimators for MPD automation, given that it is far less common compared with simpler Newtonian models used for these purposes.

Remark 2. Using mixture parameters and variables μ_m, ρ_m, and v_m is a common approach to extend liquid frictional models to two-phase flows. Likewise, we have used a mixture-behavior index n_m to be able to use the power-law model for two-phase-flow scenarios.

The DFM is completed by four other equations to be, potentially, solvable uniquely. These, often known as the closure laws, are expressed as

$$p-p_0-c_l^2(\rho_l-\rho_0)=0, \quad \ldots\ldots (7a)$$

$$p-c_g^2\rho_g=0, \quad \ldots\ldots (7b)$$

$$\alpha_l+\alpha_g-1=0, \quad \ldots\ldots (7c)$$

$$v_g-v_l-\ \Phi(u)=0, \quad \ldots\ldots (7d)$$

where p_0, ρ_0, c_l, and c_g are the reference pressure, liquid reference density, sound velocity in the liquid, and sound velocity in the gas, respectively. Eqs. 7a and 7b are, respectively, known as the equations of state (EOSs) for the liquid and gas. An EOS describes the state of matter in terms of physical variables such as temperature, density, and pressure. EOSs can be rather complex in general, but we here use linear variants approximating only the relation between pressure and density, as in Eqs. 7a and 7b. We note that these equations still capture the liquid and gas compressibility. Moreover, the volume balance between the phases is imposed by Eq. 7c, and the slip law (Eq. 7d) describes the relative velocity between the two phases depending on the function $\Phi(\cdot)$. Here, the slip law is given by (Ishii and Hibiki 2011)

$$\Phi(u)=C_0(u)v_m+V_d(u)-v_l, \quad \ldots\ldots (8)$$

where $C_0(\cdot)$ and $V_d(\cdot)$ are the distribution parameter and drift velocity, respectively. Several descriptions, which are mostly obtained using experiments and function fitting, for these parameters can be found in the literature. Depending on well conditions, mud properties, and expected drilling scenarios, a particular description of these parameters can be selected to be used in the hydraulics model, assuming only bubbly and slug flows. For a review of a variety of descriptions for these parameters and their validity conditions, see Bhagwat and Ghajar (2014).

It can be shown that the DFM admits three distinct eigenvalues in a wide region of the variable space (Evje and Fjelde 2002). These eigenvalues are $\lambda_1=v_g$, $\lambda_2=v_g-c_m$, $\lambda_3=v_g+c_m$, with $c_m(u)$ being the sound velocity in the mixture. Currently, no exact analytical expression is available for $c_m(u)$. Thus, we use an approximation of $c_m(u)$ based on the local definition of the bulk moduli,

$$c_m(u)=\sqrt{\frac{\beta_m(u)}{\rho_m(u)}}, \quad \ldots\ldots (9)$$

where β_m is the mixture bulk modulus, defined as $\beta_m=\dfrac{\beta_l\beta_g}{\alpha_l\beta_g+\alpha_g\beta_l}$, with $\beta_g=p$ and $\beta_l=c_l^2\rho_l$ being the bulk moduli of gas and liquid, respectively (Kaasa et al. 2012; Aarsnes et al. 2016a).

MPD Description and Hydraulics Modeling

Consulting Fig. 1, an MPD system can be simply regarded as two equivalent hydraulic-transmission lines (or simply pipes) that are connected through a drill bit in the middle and one of which ends up with a controllable choke valve. The exposed zone of the annulus (the so-called openhole section) is susceptible to gas and liquid influx from the surrounding formations that might potentially contain hydrocarbons. Therefore, to have a good description of the flow and pressure transients along the flow path, it is necessary to use a multiphase-flow model for the annulus. However, except in some specific drilling operations, such as operations performed in underbalanced drilling, it is quite reasonable to use a single-phase-flow model to describe the flow in the drillstring.

Hydraulics Modeling. The DFM, as in Eq. 1, can be used only for the description of the flow lines with constant cross-sectional area, while in practice there are variations in the cross-sectional area of the flow path because of changes in the diameter of pipes and open hole that affect the flow behavior. This urges the use of a modified version of the DFM that accounts for the variations in the cross-sectional area. The modified DFM for the annulus is (Rommetveit and Vefring 1991)

$$\frac{\partial(A_aq_a)}{\partial t}+\frac{\partial f_a(A_aq_a)}{\partial x}=A_aS_a+\frac{\partial A_a}{\partial x}P_a, \quad \ldots\ldots (10)$$

where $A_a(x)$ is the cross-sectional area of the annulus, and we have denoted $P_a:=[0,0,p_a]^T$. In this context, sub/superscripts a and d refer to the annulus and drillstring, respectively. Compared with the model (Eq. 1), changes in the cross-sectional area lead especially to the term $P_a\partial A_a/\partial x$. We should note that t, x, q_a, $f_a(\cdot)$, and S_a are the same as in Eq. 1, computed from the variables in the annulus. In

the annulus, as illustrated in Fig. 1, $x=0$ marks the well bottom and $x=L$ is a point in the annulus that is in the same level as the choke. Moreover, $D_a = D_{in} - d_o$, with D_{in} being the diameter of the annulus and d_o being the outer diameter of the drillstring, and $\theta_a(x) = -\theta(L-x)$.

As will be explained in later sections, we need to switch between the primitive variables u_a and the conservative ones q_a to numerically solve the model under development. On the basis of the closure laws in Eq. 7 and also the relation between the vectors q_a and u_a, as in Eq. 2, we derive a relation for the pressure in terms of conservative variables,

$$p_a = \frac{-b + \sqrt{b^2 - 4d}}{2}, \quad \ldots\ldots (11)$$

where $b = \rho_0 c_l^2 - p_0 - q_{a,1} - c_g^2$ and $d = -(\rho_0 C_l^2 - p_0) c_g^2 q_{a,2}$. Next, given the pressure from Eq. 11, Eqs. 7a and 7b can be used to compute ρ_l and ρ_g, respectively. Next, the definition of q_a leads to expressions for the volume fractions,

$$\alpha_l = \frac{q_{a,1}}{\rho_l}, \quad \alpha_g = \frac{q_{a,2}}{\rho_g}. \quad \ldots\ldots (12)$$

Next, we can compute v_l using

$$v_l = \frac{q_{a,3}(1 - C_0\alpha_g) - q_{a,2} V_d}{q_{a,1} + C_0 \alpha_g q_{a,2}}. \quad \ldots\ldots (13)$$

Then, from the slip law (Eq. 7d), with Eq. 8, we obtain

$$v_g = \frac{C_0 \alpha_l v_l + V_d}{1 - C_0 \alpha_g}. \quad \ldots\ldots (14)$$

Remark 3. Depending on the choice of $C_0(u)$ and $V_d(u)$, if these parameters are dependent on v_l and v_g, then Eqs. 13 and 14 can become nonlinear equations with respect to v_l and v_g, which need to be solved simultaneously using nonlinear solvers. However, these are often independent of v_l and v_g.

As already mentioned, the main reason for using a two-phase model for the annulus is to enable modeling of a gas influx from the formation into the annulus. On the contrary, it is reasonable to use a single-phase model for describing the flow behavior inside the drillstring. It is worth mentioning that there are certain drilling operations, such as operations in underbalanced drilling, where some rate of gas is intentionally injected into the drillstring. This gas injection in turn gives rise to a two-phase medium in the drillstring. An isothermal Euler equation accounting for the variations in the cross-sectional area describes the flow behavior in the drillstring,

$$\frac{\partial (A_d q_d)}{\partial t} + \frac{\partial f_d (A_d q_d)}{\partial x} = A_d S_d + \frac{\partial A_d}{\partial x} P_d, \quad \ldots\ldots (15)$$

where $f_d(A_d q_d) = [A_d \rho v, A_d \rho v^2 + A_d p_d]^T$, $S_d(u_d, t, x) = [0, s_d(u_d, t, x)]^T$, $P_d := [0, p_d]^T$. Moreover, $\rho = \rho(t,x)$, $v = v(t,x)$, $p_d = p_d(t,x)$ are the mud density, velocity, and pressure profiles along the drillstring. The vectors of primitive and conservative variables are indicated by $u_d = [\rho, v, p_d]^T$ and $q_d = [\rho, \rho v]^T$, respectively. Moreover, $A_d(x)$ is the cross-sectional area of the drillstring. For the drillstring, $x=0$ marks a point in the drillstring that is at the same level as the pump, whereas $x=L$ marks its outlet at the bit. To avoid unnecessary notational complexities, we do not use a subscript to refer to the primitive variables in the drillstring, except for the pressure. As before, s_d is the source term acting on the flow in the drillstring, and the same model as in Eq. 3 is used to determine it, with the mixture variables and parameter reducing to liquid variables. Moreover, we have $D_d = d_{in}$, with d_{in} being the inner diameter of the drillstring, and $\theta_d(x) = \theta(x)$. The EOS considered for the liquid in the drillstring is the same as Eq. 7a, the one used in the annulus.

Remark 4. It should be noted that Eq. 15 can be obtained from Eq. 10 by setting $\alpha_g = 0$.

Boundary Conditions. To potentially be able to solve Eqs. 10 and 15 uniquely, one needs to specify a set of boundary conditions. In this regard, a careful observation of Fig. 1 reveals that the hydraulics behavior of an MPD system is largely dictated by three main physical boundary conditions, which are the boundaries at the drillstring inlet, the bit together with the behavior of the formations around the openhole, and the choke valve, as the annulus outlet.

The boundary condition at the drillstring inlet is expressed in a general form as

$$f_{ibc}[\rho(t,0), v(t,0), t] = 0, \quad \ldots\ldots (16)$$

where $f_{ibc}(\cdot,\cdot,\cdot)$ is the boundary condition at the drillstring inlet, and it is determined depending on the ongoing drilling operation. For example, during normal operations, when the drillstring is connected to the mud pump, we can define

$$f_{ibc} := A_d(0)\rho(t,0)v(t,0) - J_p(t), \quad \ldots\ldots (17)$$

where $J_p(t)$ denotes the mass-flow rate of the mud pumped into the drillstring. It should be noted that in practice we are often provided the pump strokes per minutes $n_p(t)$ rather than the mass-flow rate. In that case, the mass-flow rate can be computed using $J_p[\rho(t,0), t] = V_p n_p(t) \rho(t,0)$, where V_p is the volume that the pump sweeps per stroke. As another example, during a bleedoff operation, an operation to slowly release the trapped pressure within the drillstring before detaching it from the topdrive, a valve equation should be used to model this boundary condition. Next, at the bottom of the well, one can write three boundary equations, consisting of the bit equation that describes the liquid-mass-flow rate through the bit in terms of the pressure drop over the bit, the liquid-mass-balance equation between both sides of the bit, and the gas balance between the formations and the annulus, respectively,

$$A_d(L)\rho(t,L)v(t,L) - c_d A_n \sqrt{2\rho(t,L) r [p_d(t,L) - p_a(t,0)]} = 0, \quad \ldots\ldots (18)$$

$$A_d(L)\rho(t,L)v(t,L)+J_r^l[p_a(t,0),p_r]-A_a(0)\alpha_l(t,0)\rho_l(t,0)v_l(t,0)=0, \quad \ldots\ldots (19)$$

$$J_r^g[p_a(t,0),p_r]-A_a(0)\alpha_g(t,0)\rho_g(t,0)v_g(t,0)=0, \quad \ldots\ldots (20)$$

where the function $r(e)=\begin{cases} e, \text{ if } e>0 \\ 0, \text{ if } e\le 0 \end{cases}$ is used to model the non-return valve installed above the bit inside the bottomhole assembly, A_n is the effective area of the bit nozzles, and c_d is the discharge coefficient. $J_r^l(\cdot,\cdot)$ and $J_r^g(\cdot,\cdot)$ represent the mass-flow rates of the liquid and gas, respectively, exchanged between the wellbore and the formations with a pressure p_r, known as the reservoir pressure. Here, we approximate these variables using a linear static reservoir model (Aarsnes et al. 2016c),

$$J_r^i=\kappa_i r[p_r-p_a(t,0)], \quad i\in\{g,l\}, \quad \ldots\ldots (21)$$

where κ_i is the production index for the phase i. Coupling with a more intricate reservoir model is also possible, and it can be substituted into Eq. 21. However, near-wellbore reservoir modeling is beyond the scope of this paper. At the top side of the annulus, the boundary condition is determined by the choke equation describing the mass-flow rate of the mixture through the choke as a function of the pressure drop over the choke (Di Meglio et al. 2011),

$$\begin{aligned} &J_c[t,u_a(t,L)]-J_{bpp}(t)-J_c^u[u_a(t,L)]=0,\\ &J_c[t,u_a(t,L)]=\sum_{i=1}^{n_c}k_{c,i}G_i[z_{c,i}(t)]\sqrt{2\rho_m(t,L)r[p_a(t,L)-p_0]}, \end{aligned} \quad \ldots\ldots (22)$$

where $k_{c,i}$, $z_{c,i}$, and $G_i(\cdot)$ are the choke-flow factor, the choke opening, and the choke characteristic of the choke valve i, respectively. n_c is the number of choke valves in the MPD setup and $J_{bpp}(t)$ is the mass-flow rate from the backpressure pump. Moreover, $J_c^u=A_a(L)\alpha_l(t,L)\rho_l(t,L)v_l(t,L)+A_a(L)\alpha_g(t,L)\rho_g(t,L)v_g(t,L)$ is the mass-flow rate upstream the choke, whereas J_c is that downstream the choke. Again, more accurate models of multiphase flow through the valve can be derived to replace Eq. 22.

The combination of Eqs. 7 through 22 constructs our MPD simulation model. Specifically, in this model, we have accounted for variations in the cross-sectional area of the flow path and also the nonlinear boundary conditions of an MPD system. The MPD model has now been specified, and next the steady-state solution of the system can be found using this model.

Steady-State Solution of the Model

Clearly, to be able to solve the MPD model derived in the preceding section, an initial condition is required. Because most of the drilling time is occupied by normal drilling operations, it is reasonable to start a simulation study from a drilling-ahead condition. In this case, the system shows steady-state behavior; therefore, all the derivatives with respect to the time variable t can be discarded from Eqs. 10 and 15, resulting in the steady-state-differential equations

$$\begin{aligned} &\frac{df_a(A_a\overline{q}_a)}{dx}=A_a\overline{S}_a+\frac{\partial A_a}{\partial x}\overline{P}_a,\\ &\frac{df_d(A_d\overline{q}_d)}{dx}=A_d\overline{S}_d+\frac{\partial A_d}{\partial x}\overline{P}_d. \end{aligned} \quad \ldots\ldots (23)$$

Now, using the closure laws (Eq. 7) together with Eq. 23, we obtain

$$\begin{aligned} &\frac{d\overline{y}_a(x)}{dx}=M_a^{-1}(\overline{y}_a)H_a(\overline{y}_a,x),\\ &\frac{d\overline{y}_d(x)}{dx}=M_d^{-1}(\overline{y}_d)H_d(\overline{y}_d,x), \end{aligned} \quad \ldots\ldots (24)$$

where $\overline{y}_d(x)=[\overline{v},\overline{\rho}]^T$, $\overline{y}_a(x)=[\overline{v}_l,\overline{v}_g,\overline{\alpha}_g,\overline{p}_a]^T$, with the macron bar (i.e., $\bar{\ }$) indicating the variables and vectors in the steady state. Moreover,

$$M_a=\begin{bmatrix} 1-\frac{\partial\Phi}{\partial\overline{v}_g} & -1-\frac{\partial\Phi}{\partial\overline{v}_l} & -\frac{\partial\Phi}{\partial\overline{\alpha}_g} & -\frac{\partial\Phi}{\partial\overline{p}_a} \\ (1-\overline{\alpha}_g)\overline{\rho}_l & 0 & -\overline{\rho}_l\overline{v}_l & \frac{\overline{v}_l(1-\overline{\alpha}_g)}{c_l^2} \\ 0 & \overline{\alpha}_g\overline{\rho}_g & \overline{\rho}_g\overline{v}_g & \frac{\overline{\alpha}_g\overline{v}_g}{c_g^2} \\ (1-\overline{\alpha}_g)\overline{\rho}_l\overline{v}_l & \overline{\alpha}_g\overline{\rho}_g\overline{v}_g & 0 & 1 \end{bmatrix}, \quad M_d=\begin{bmatrix} \overline{\rho} & \overline{v} \\ \overline{\rho v} & c_l^2 \end{bmatrix},$$

$$H_a=\overline{S}_a-\frac{dA_a}{dx}\begin{bmatrix} 0 \\ \frac{(1-\overline{\alpha}_g)\overline{\rho}_l\overline{v}_l}{A_a} \\ \frac{\overline{\alpha}_g\overline{\rho}_g\overline{v}_g}{A_a} \\ 0 \end{bmatrix}, \quad H_d=\overline{S}_d-\frac{1}{A_d}\frac{dA_d}{dx}\begin{bmatrix} \overline{\rho v} \\ 0 \end{bmatrix}, \quad \ldots\ldots (25)$$

with $\Phi(u)$ as in Eq. 8. The boundary conditions of the ordinary differential equation (Eq. 24) are given by the physical boundary conditions (Eqs. 17, 18, and 22) in the steady-state conditions,

$$(A_d\overline{\rho v})|_{x=0} - \overline{J}_p = 0,$$
$$(A_d\overline{\rho v})|_{x=L} - [A_a(1-\overline{\alpha}_g)\overline{\rho}_l\overline{v}_l]|_{x=0} + J_f^l[\overline{p}_a(0),\overline{p}_r] = 0,$$
$$J_f^g[\overline{p}_a(0),\overline{p}_r] - (A_a\overline{\alpha}_g\overline{\rho}_g\overline{v}_g)|_{x=0} = 0,$$
$$(A_d\overline{\rho v})|_{x=L} - A_n c_d\sqrt{2\overline{\rho}(L)r[\overline{p}_d(L) - \overline{p}_a(0)]} = 0,$$
$$(A_a\overline{\alpha}_l\overline{\rho}_l\overline{v}_l + A_a\overline{\alpha}_g\overline{\rho}_g\overline{v}_g)|_{x=L} + \overline{J}_{bpp} - \sum_{i=1}^{n_c} k_{c,i}G_i(\overline{z}_{c,i})\sqrt{2\overline{\rho}_m(L)r[\overline{p}_a(L) - p_0]} = 0. \quad \ldots\ldots\ldots\ldots\ldots\ldots\ldots\ldots\ldots\ldots (26)$$

Eqs. 24 and 26 construct a two-point boundary-value problem in terms of x as the independent variable.

Note that the presence of dA/dx, which contains impulses caused by area discontinuities in $A(x)$, in the steady-state equations (Eq. 24) causes discontinuities in the steady-state solution. After we have initialized our problem by solving Eq. 24, we start with the numerical implementation of the model in the sequel.

The developed model in this paper includes the system dynamics and aspects that are essential to the control performance. Considering only the control-relevant aspects of the system in the model keeps its complexity relatively low, such that it permits, for example, a semianalytical assessment of its dynamical properties (an assessment that relies partially on theoretical analyses and partially on numerical analyses). For instance, semianalytical analyses are used in Di Meglio (2011). This type of assessment can be computationally expensive, if not impossible, in the case of high-complexity models. Moreover, simulation studies performed during the controller design might need to be performed several times. Thus, it is important for these simulations to run quickly. Moreover, the relatively low complexity of the model will allow designers and engineers to more easily identify the reason for or the source of problems in the case of poor simulation results.

Numerical Implementation

The MPD model derived previously cannot be solved analytically because of its complexity (e.g., infinite-dimensional nature and nonlinearities). To solve and then use this model for simulation purposes, we use a numerical scheme that is based on a finite-volume-method discretization. As illustrated in **Fig. 2,** in the finite-volume method (LeVeque 2002), the spatial domain of a hyperbolic partial-differential equation (PDE) is divided into a finite number of control volumes or cells. All the variables are assumed to have a predefined distribution in each control volume. As illustrated in Fig. 2, the spatial domain is discretized into N cells denoted by $G_i = (x_{i-1/2}, x_{i+1/2})$, $i = \{1, 2, \ldots, N\}$, of length Δx, with $x_{i+1/2} = i\Delta x$ as the ith cell interface and $x_i = (i - 1/2)\Delta x$ marking the middle point of that cell. The variable U_i^n [Q_i^n] is an approximation of the spatial average of the vector $u(n\Delta t, x)$ [$q(n\Delta t, x)$] over G_i and the approximate variables at the right- and left-hand sides of each interface are indicated by U^- and U^+, respectively. Here, Δt is the discretization timestep size. A finite-volume Godunov-type method has the general form (LeVeque 2002)

$$Q_i^{n+1} = Q_i^n - \frac{\Delta t}{\Delta x}[F(U_{i+1/2}^{+*}, U_{i+1/2}^-) - F(U_{i-1/2}^+, U_{i-1/2}^{-*})] + \Delta t S_i^n, \quad \ldots\ldots\ldots\ldots\ldots\ldots\ldots\ldots\ldots\ldots\ldots\ldots\ldots\ldots\ldots\ldots (27)$$

where $F(\cdot,\cdot)$, a conventional numerical flux function assuming a fixed cross-sectional area, is determined by the numerical scheme, and $S_i^n = S(U_i^n, n\Delta t, x_i)$ is the discretized source term. A starred variable U^*, yet to be computed, is an update of the variable U that accounts for variations in the cross-sectional area of the flow. Note that because the same formula as in Eq. 27 is used for solving both Eqs. 10 and 15, the sub/superscripts a and d are omitted for readability. The timestep size Δt is determined using the Courant-Friedrichs-Lewy (CFL) condition (Courant et al. 1967). In particular, the numerical implementation of the DFM (Eq. 1) has been extensively studied in the last few decades (Fjelde and Karlsen 2002). These studies mostly aim at developing accurate but computationally low-cost numerical schemes for computing the numerical flux function.

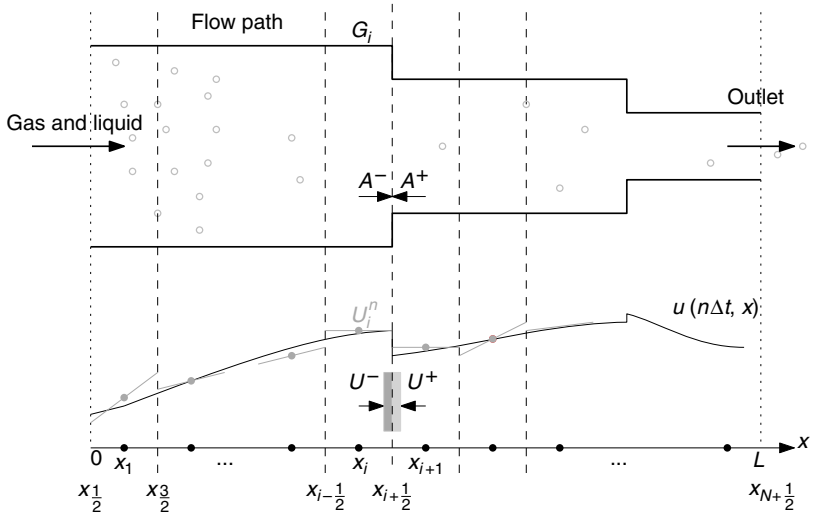

Fig. 2—Illustration of a spatial discretization performed in the finite-volume method.

To treat the variations in the cross-sectional area of the flow path of the MPD model, the method proposed by Kröner and Thanh (2005) for Eq. 15 and an extension of that method proposed by Abbasi et al. (2019) for the modified DFM (Eq. 10) are exploited here to compute the variables with asterisk symbols in Eq. 27. In this method, we use a coordinate transformation that gives the equivalent values of the variables in a cell if the geometry of that cell changes. In particular, when updating the variables in the cell G_i, we assume

that the cells G_{i-1} and G_{i+1} have the same geometries as G_i and use this transformation to compute the equivalent of the variables in those cells, considering this change of geometry. In this way, we are still able to use a Godunov setting with numerical flux functions as in Eq. 27 to numerically solve our MPD simulation model. Following this approach, $U_d^{+*} = [\rho^{+*}, v^{+*}]^T$ of the interface $i + 1/2$ in the drillstring is obtained through a nonlinear coordinate transformation that is given in terms of a system of equations,

$$\rho^{+*}v^{+*}A_d^- - \rho^+ v^+ A_d^+ = 0,$$
$$(v^{+*})^2 - (v^+)^2 + c_l^2 \ln\left(\frac{\rho^{+*}}{\rho^+}\right)^2 = 0, \qquad (28)$$

where A^- and A^+ denote, as illustrated in Fig. 2, the cross-sectional area A immediately at the left- and right-hand sides of an interface, respectively. Moreover, U_d^{-*} of the interface $i - 1/2$ is obtained by replacing the superscripts $+$ and – with – and $+$, respectively, in Eq. 28 and then solving the resulting equation. Next, U_a^{+*} for the DFM of the annulus is obtained by a coordinate transformation given by Eq. 29 together with closure relations Eqs. 7a through 7d and 8,

$$\left(\alpha_l^{+*}\rho_l^{+*}v_l^{+*}\right)A_a^- - \left(\alpha_l^{+}\rho_l^{+}v_l^{+}\right)A_a^+ = 0,$$
$$\left(\alpha_g^{+*}\rho_g^{+*}v_g^{+*}\right)A_a^- - \left(\alpha_g^{+}\rho_g^{+}v_g^{+}\right)A_a^+ = 0,$$
$$\frac{\alpha_l^{+*}\rho_l^{+*}}{\rho_g^{+*}}\left(\frac{v_l^{+*}}{2}\right)^2 + \alpha_g^{+*}\left(\frac{v_g^{+*}}{2}\right)^2 - \frac{\alpha_l^{+}\rho_l^{+}}{\rho_g^{+}}\left(\frac{v_l^{+}}{2}\right)^2 - \alpha_g^{+}\left(\frac{v_g^{+}}{2}\right)^2 + c_g^2 \ln\left(\frac{\rho_g^{+*}}{\rho_g^{+}}\right)^2 = 0. \qquad (29)$$

As before, U_a^{-*} of the interface $i - 1/2$ is obtained by replacing $+$ and – in Eq. 29 with – and $+$, respectively.

Remark 5. A close observation of Eq. 28 reveals that variations in the pressure profile $p_d(t,x)$ in the drillstring caused by changes in the cross-sectional area at the location of these changes are not significant. This is mainly because the mud velocity v in the drillstring is far smaller than the sound velocity c_l. On the contrary, when there is gas inside the annulus, variations in the cross-sectional area can cause considerable variations in the pressure. Given this explanation, without losing much accuracy, we can assume that $\rho^{+*} = \rho^+$ for the drillstring and solve only the mass-balance equation of Eq. 28, which is linear, for computing v^{+*}.

After computing Q_i^{n+1} from Eq. 27, the vector of primitive variables is computed using Eqs. 11 through 14. Then, if a first-order scheme is used, a uniform distribution is considered for the variables $u(n\Delta t, x)$ over a cell G_i, thus

$$\hat{u}(n\Delta t, x) = U_j^n, \quad x \in (x_{i-\frac{1}{2}}, x_{i+\frac{1}{2}}). \qquad (30)$$

When a second-order scheme is used, this approximation is obtained by a linear interpolation as

$$\hat{u}(n\Delta t, x) = U_j^n + (u_x)_j^n (x - x_i), \quad x \in (x_{i-\frac{1}{2}}, x_{i+\frac{1}{2}}), \qquad (31)$$

where $(u_x)_j^n$ is an approximation of the exact derivatives $\partial u(n\Delta t, x)/\partial x$ at $x = x_j$, computed using a flux limiter (Sweby 1984).

Remark 6. We reasonably assume that $A(x)$ is piecewise continuous, with a discontinuity occurring only at a cell interfaces such that $A(x)$ is constant in each cell G_i [i.e., for $x \in (x_{i-1/2}, x_{i+1/2})$, $i = 1, 2, \ldots, N$].

In the next subsection, we explain how to combine the implicit boundary conditions of the problem with the numerical scheme used for updating the internal domains of the model.

Boundary-Conditions Treatment. Expanding the scheme (Eq. 27) for $i = 1$ and $i = N$ reveals explicit dependencies on U_0 and U_{N+1}, and also implicit dependencies on U_{-1}, U_{N+2} for the case of second-order schemes. These variables are required to incorporate the boundary conditions of the boundary-value problem in the described scheme in the preceding section. Extrapolation is a common method for determining the boundary variables. It is effective and can provide accurate results if there are no source terms in the model (Prebeg et al. 2015). However, it lacks a sound theoretical support and can cause large spikes in the solution in the presence of source terms. Contrary to extrapolation, a method known as the characteristics-based method (Cook et al. 2018) offers more accurate and reliable solutions and it also has a more reliable theoretical foundation. This method involves breaking a two-point boundary-value problem into two initial value problems and solving those separately at their respective boundaries. Now, by using a nonlinear coordinate transformation and approximations, the DFM with the closure laws (Eqs. 7a through 7d) can be decomposed into its characteristic equations. In this form, two of the PDEs describe the propagation of the pressure waves, also called fast dynamics of the DFM, inside the domain, and one PDE, called the slow dynamics, describes the migration of the gas phase. For the DFM (characterizing flow in the annulus), these relations come in the following form (Fjelde and Karlsen 2002),

$$\alpha_g(1 - C_0\alpha_g)\frac{d_1 p_a}{d_1 t} + p_a \frac{d_1}{d_1 t}\alpha_g = 0, \qquad (32)$$

$$\frac{d_2 p_a}{d_2 t} - \rho_l c_m (v_g - v_l)\frac{d_2 \alpha_g}{d_2 t} - \rho_l \alpha_l (v_g - v_l + c_m)\frac{d_2 v_l}{d_2 t} = (v_g - v_l + c_m)s_a, \qquad (33)$$

$$\frac{d_3 p_a}{d_3 t} + \rho_l c_m (v_g - v_l)\frac{d_3 \alpha_g}{d_3 t} - \rho_l \alpha_l (v_g - v_l - c_m)\frac{d_3 v_l}{d_3 t} = (v_g - v_l - c_m)s_a, \qquad (34)$$

where in this case we have defined $\frac{d_i}{d_i t} := \frac{\partial}{\partial t} + \lambda_{a,i}\frac{\partial}{\partial x}$, $i = 1, 2, 3$, which is a directional derivative along the vector $V = [1, \lambda_{a,i}]^T$, with $\lambda_{a,i}$ being an eigenvalue of the DFM of the annulus. Eqs 32 through 34 correspond to the gas-volume wave traveling at a speed $\lambda_{a,1} = v_g$ downstream the annulus, the pressure waves propagating at $\lambda_{a,2} = v_l - c_m$ upstream the annulus, and the pressure wave traveling at a speed of $\lambda_{a,3} = v_l + c_m$ toward the choke, respectively. The characteristic relations of the isothermal Euler equation describing the single-phase flow in the drillstring are given by

$$\frac{\partial p_d}{\partial t} - \lambda_{d,1}\frac{\partial p_d}{\partial x} - c_l\rho\frac{\partial v}{\partial t} - c_l\rho\lambda_{d,1}\frac{\partial v}{\partial x} = c_l s_d, \quad \ldots\ldots (35)$$

$$\frac{\partial p_d}{\partial t} + \lambda_{d,2}\frac{\partial p_d}{\partial x} + c_l\rho\frac{\partial v}{\partial t} + c_l\rho\lambda_{d,2}\frac{\partial v}{\partial x} = -c_l s_d, \quad \ldots\ldots (36)$$

where Eq. 35 corresponds to the pressure wave traveling upstream the flow with a velocity of $\lambda_{d,1} = v - c_l$, while Eq. 36 corresponds to the pressure wave traveling the opposite direction at a velocity of $\lambda_{d,2} = c_l + v$.

Remark 7. Note that the characteristic relations in Eqs. 32 through 34 are obtained under several simplifying assumptions, such as an incompressible liquid phase, $\partial C_0(u)/\partial u = 0$ and $\partial V_d(u)/\partial u = 0$, and that $\alpha_g\rho_g \ll \alpha_l\rho_l$ holds, because otherwise the derivation of such relations is highly challenging, if not impossible. Naturally, these assumptions lead to some degree of inaccuracy in the computation of the boundary variables. Nonetheless, for small gas volume fractions α_g (less than 0.25) at the boundaries, these assumption are rather realistic, especially when MPD operations are supported by high-performance kick detectors and pressure-control systems that prevent large gas kicks. It is mentioned that the relations in Eqs. 35 and 36 are exact.

In the remainder of this section, we propose a method for computing the boundary variables using the characteristic relations of Eqs. 32 through 36 together with the physical boundary conditions introduced previously.

We solve the drillstring inlet boundary condition in Eq. 16 together with the characteristic relation (Eq. 35), forming an initial value problem as

$$\begin{aligned} &f_{ibc}[\rho(t,0), v(t,0), t] = 0,\\ &\frac{\partial p_d}{\partial t} - \lambda_{d,1}\frac{\partial p_d}{\partial x} - c_l\rho\frac{\partial v}{\partial t} - c_l\rho\lambda_{d,1}\frac{\partial v}{\partial x} = c_l s_d. \end{aligned} \quad \ldots\ldots (37)$$

This algebraic PDE, if solved at $x=0$, gives $u_d(t,0) = [v(t,0), \rho(t,0)]^T$. However, finding the analytical solution of this nonlinear algebraic PDE is challenging. Therefore, we solve Eq. 37 numerically by performing a first-order Euler discretization (both spatial and temporal) on Eq. 37, yielding

$$\begin{aligned} &f_{ibc}(\rho_0^n, v_0^n, n\Delta t) = 0,\\ &\frac{p_{d,0}^n - p_{d,0}^{n-1}}{\Delta t} - c_l\rho_1^{n-1}\frac{v_0^n - v_0^{n-1}}{\Delta t} = -(\lambda_{d,1})_1^{n-1}\frac{p_{d,0}^{n-1} - p_{d,1}^{n-1}}{\Delta x} - c_l(\rho\lambda_{d,1})_1^{n-1}\frac{v_0^{n-1} - v_1^{n-1}}{\Delta x} + c_l s_d[U_{d,1}^{n-1}, (n-1)\Delta t, 0], \end{aligned} \quad \ldots\ldots (38)$$

where the variables ρ_0^n and v_0^n, the solutions of Eq. 38, are approximations of $\rho(n\Delta t, 0)$ and $v(n\Delta t, 0)$, respectively, and the notation $(\cdot)_j^i$ stands for the term inside the parentheses evaluated at the time instance i and the point x_j in the special domain. The resulting nonlinear algebraic equation Eq. 38, together with the EOS (Eq. 7a), can be solved with a proper zero-finder algorithm, such as a Newton solver. After this equation is solved, we can compute $U_{d,0}^n = [v_0^n, \rho_0^n]^T$ and $Q_{d,0}^n = [\rho_0^n, \rho_0^n v_0^n]^T$, as required in Eq. 27 for the drillstring. At the bottom of the well, we take a similar approach. At this boundary, there are couplings between the boundary variables in the annulus and those in the drillstring, and nine unknown boundary variables in total with seven boundary equations and closure laws. These together with the characteristic equations (Eqs. 36 and 33) construct an initial value problem that is solved numerically at this boundary to compute the boundary vectors $U_{d,N+1}^n$ and $U_{a,0}^n$ (as well as $Q_{d,N+1}^n$ and $Q_{a,0}^n$). However, using a numerical method similar to the one described previously is computationally expensive because it involves solving a nine-dimensional nonlinear algebraic equation. Moreover, it can cause numerical oscillations when the flow through the bit is close to zero, which is the case during a pipe-connection operation. Therefore, here we connect the two boundaries at both sides of the bit through an intermediate ordinary-differential equation (for the derivation, see Appendix B),

$$\dot{z}(t) \simeq \begin{cases} \xi[z(t), \Delta p_{dh}(t)], & \text{for} \quad z(t) > 0,\\ \max\{0, \xi[z(t), \Delta p_{dh}(t)]\}, & \text{for} \quad z(t) = 0 \end{cases} \quad \ldots\ldots (39)$$

where $\Delta p_{dh}(t) = p_d(t, L - \Delta l/2) - p_a(t, \Delta l/2)$, and

$$\xi = \frac{2A_d(L)A_a(0)}{\Delta l[A_d(L) + A_a(0)]}\left[\Delta p_{dh} - \frac{z^2}{2\rho(t, L - \Delta l/2)(A_a c_d)^2} + \frac{\tilde{s}_a}{A_d(0)} + \frac{\tilde{s}_d}{A_a(L)}\right], \quad \ldots\ldots (40)$$

with $z(t)$ being an approximation of the mass flow rate through the bit $J_{\text{bit}}(t)$, and $\tilde{s}_a$ and $\tilde{s}_d$ as in Appendix B. The operator $\max(\cdot,\cdot)$ in Eq. 39 is used to account for the non-return valve installed in the drillstring to prevent a backflow from the annulus into the drillstring, and we take Δl as a parameter that determines the inertia of the dynamics of $z(t)$. Now, using the other characteristic relation in the drillstring and performing an Euler discretization over space and time, we can approximately compute the drillstring boundary variables at the bit by solving

$$\begin{aligned} &z^n - A_d(L)\rho_{N+1}^n v_{N+1}^n = 0,\\ &\frac{p_{d,N+1}^n - p_{d,N+1}^{n-1}}{\Delta t} - c_l\rho_N^{n-1}\frac{v_{N+1}^n - v_{N+1}^{n-1}}{\Delta t} = (\lambda_{d,2})_N^{n-1}\frac{p_{d,N}^{n-1} - p_{d,N+1}^{n-1}}{\Delta x} + c_l(\rho\lambda_{d,2})_N^{n-1}\frac{v_N^{n-1} - v_{N+1}^{n-1}}{\Delta x} - c_l s_d[U_{d,N}^{n-1}, (n-1)\Delta t, L - \Delta x/2], \end{aligned} \quad \ldots\ldots (41)$$

where v_{N+1}^n and ρ_{N+1}^n are approximations of the boundary variables $v(t,L)$ and $\rho(t,L)$, respectively, and z^n, an approximation of $z(n\Delta t)$, is obtained from the time discretization of Eq. 39 using an Euler method,

$$\begin{aligned} \chi^j \quad &= \chi^{j-1} + \begin{cases} \Delta t_z\xi(\chi^{j-1}, \Delta p_{dh}^{n-1}), & \text{for} \quad \chi^{j-1} > 0,\\ \Delta t_z\max[0, \xi(\chi^{j-1}, \Delta p_{dh}^{n-1})], & \text{for} \quad \chi^{j-1} = 0, \end{cases} \qquad j = \{1, ..., m\}.\\ z^n &:= \chi^m, \end{aligned} \quad \ldots\ldots (42)$$

where χ is an auxiliary variable such that $\chi^0 = z^{n-1}$ and Δt_z is the corresponding discretization timestep size. Note that, to avoid numerical oscillations when the timestep Δt is large, we can design Δt_z to be smaller than Δt. To this end, we set $\Delta t_z = \Delta t/m$, $m \in \mathbb{N}$, where m is chosen to be large enough.

Analogously, we can compute $U_{a,0}^n$, as an approximation of $u_a(n\Delta t, 0)$, by solving the following system of nonlinear algebraic equations as a result of spatial and temporal discretization of Eq. 33 using the Euler method with Eqs. 19 and 20,

$$\begin{aligned}
&z^n + J_r^l(p_{a,0}^n, p_r) - A_a(0)(\alpha_l \rho_l v_l)_0^n = 0,\\
&J_r^g(p_{a,0}^n, p_r) - A_a(0)(\alpha_g \rho_g v_g)_0^n = 0,\\
&\frac{p_{a,0}^n - p_{a,0}^{n-1}}{\Delta t} - [\rho_l c_m(v_g - v_l)]_1^{n-1} \frac{\alpha_{g,0}^n - \alpha_{g,0}^{n-1}}{\Delta t}\\
&\qquad - [\rho_l \alpha_l (v_g - v_l + c_m)]_1^{n-1} \frac{v_{l,0}^n - v_{l,0}^{n-1}}{\Delta t} = -(\lambda_{a,2})_1^{n-1} \frac{p_{a,1}^{n-1} - p_{a,0}^{n-1}}{\Delta x} + [\lambda_{a,2} \rho_l c_m (v_g - v_l)]_1^{n-1} \frac{\alpha_{g,1}^{n-1} - \alpha_{g,0}^{n-1}}{\Delta x}\\
&\qquad + [\lambda_{a,2} \rho_l \alpha_l (v_g - v_l + c_m)]_1^{n-1} \frac{v_{l,1}^{n-1} - v_{l,0}^{n-1}}{\Delta x} + (v_g - v_l + c_m)_1^{n-1} s_a[U_{a,1}^{n-1}, (n-1)\Delta t, 0]. \qquad (43)
\end{aligned}$$

Note that the above equations (Eq. 43) need to be solved together with the closure laws to return (generally) a unique solution. After solving Eqs. 41 and 43, we can compute $Q_{d,N+1}^n$ and $Q_{a,0}^n$. At the choke boundary, the initial value problem consists of the choke equation (Eq. 22), and all closure laws of the DFM (Eqs. 7a through 7d) together with the two characteristic equations (Eqs. 32 and 34). This problem is approximated in terms of a nonlinear algebraic equation, similar to Eq. 38, using a first-order Euler discretization over space and time domains. The solution of the resulting algebraic equation is then used to compute $U_{a,N+1}^n$ and $Q_{a,N+1}^n$.

Remark 8. If a second-order scheme is used, in addition to the boundary vectors $U_{a,0}$ and $U_{a,N+1}$, the vectors $U_{a,-1}$ and $U_{a,N+2}$ also need to be determined. Although these variables are less crucial than the boundary variables for the accuracy of the MPD model, the way we compute these can have a significant effect on the solution. A common approach in this regard is to assume that $U_{a,-1} = U_{a,0}$ and $U_{a,N+2} = U_{a,N+1}$. However, one can use more advanced approaches, such as the one proposed by Prebeg et al. (2017), which comes at a higher computational expense.

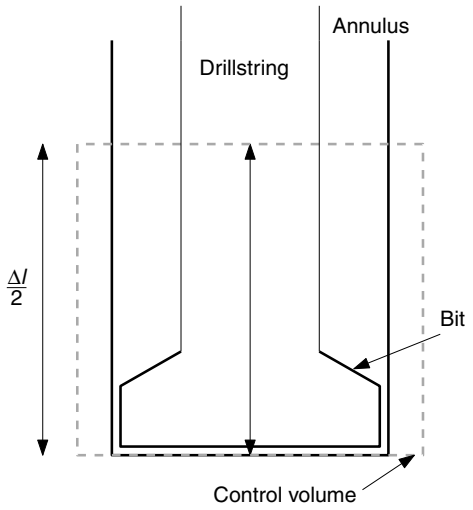

Fig. 3—Schematic of the control volume assumed over the bit to facilitate solving the boundary equations at the bit.

Field-Data Comparisons and Simulation Studies of Industry-Relevant Scenarios

To evaluate the predictive capabilities of the simulation model and the performance of the proposed numerical implementation of the model, simulations and model validations against experimental data are performed in this section.

Comparisons with Field Data. We have performed comparisons for single-phase-flow scenarios between the hydraulics model presented in this paper and field data obtained during commissioning tests of an MPD operation on a real drilling well. These tests were performed after running casing and before resuming drilling ahead at the length of 1647 m to adjust the MPD control system. The geometries of the drillstring and wellbore are reported in **Fig. 4.** The other parameters used in the model are listed in **Table 1.** The considered measurements correspond to a time period when the drillstring was stationary. In this experiment, the mass flow of the mud pumped into the drillstring varies between low, medium, and high values at different rates.

In this paper, instead of identifying $G_i(z_{c,i})$ as a function of $z_{c,i}$, we approximate it as a function of time [i.e., we compute the implicit choke characteristic $G(t)$ from the measurements and use it in our simulations]. In particular, to approximately compute $G(t)$, we use the relation

$$G(t) = \sum_{i=1}^{2} G_i(z_{c,i}) \simeq \frac{J_c(t)}{k_{c,1}\sqrt{2\rho_c(t) r[p_c(t) - p_0]}}, \qquad (44)$$

where $p_c(t) = p_a(t, L)$ and $\rho_c(t) = \rho_a(t, L)$ are the measured pump pressure and flow density upstream of the choke, and it is assumed that $k_{c,2} = k_{c,1}$. The choke flow $J_c(t)$ is also a measured variable in Eq. 44. We note that this relation is directly obtained from the choke equation in Eq. 22. The pump-flow rate together with the choke-opening signals and implicit choke characteristic $G(t)$ are reported in **Fig. 5.**

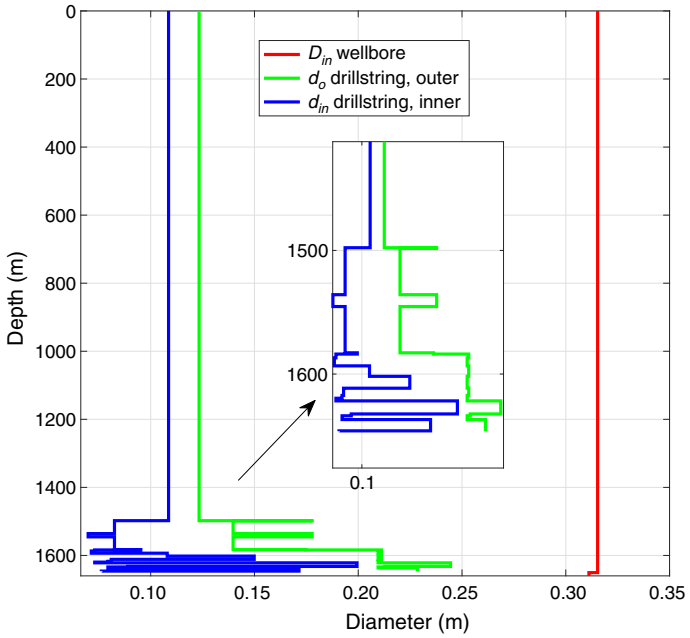

Fig. 4—Diameter of the annulus and drillstring of the drilling well used in the model-validation studies.

Parameter	Symbol	Value	Unit
Length of the well	L	1647	m
Average well inclination	$\overline{\theta}$	1.08	rad
Liquid-bulk modulus	β_l	0.94×10^{9}	Pa
Reference pressure	p_0	10^{5}	Pa
Liquid density at p_0	ρ_0	1210	kg/m^3
Number of chokes	n_c	2	–
Choke-flow factor	$k_{c,1}$	0.0026	m^2
Choke-flow factor	$k_{c,2}$	0.0026	m^2
Liquid viscosity	μ_l	0.177	Pa·s
Liquid-behavior index	n_l	0.93	–
Bit-nozzle area	A_n	5.69×10^{-4}	m^2
Bit-discharge coefficient	c_d	0.8	–

Table 1—Parameters used in the hydraulics model for model validation.

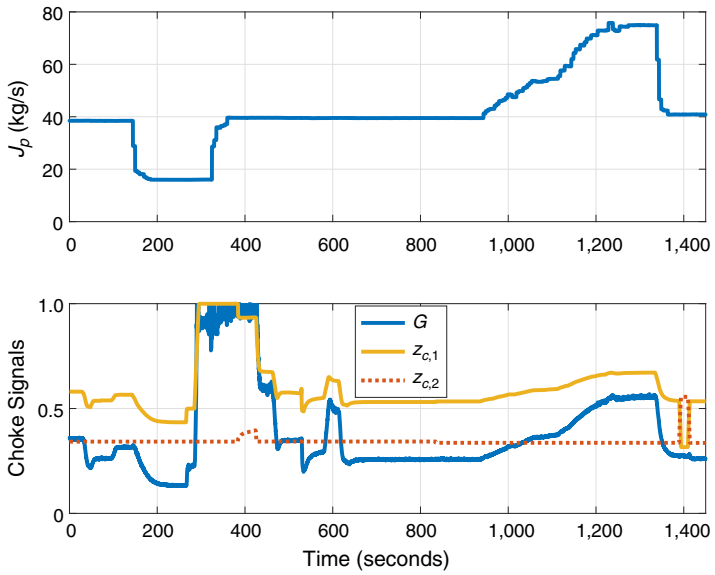

Fig. 5—Field data: (top) the pump-mass-flow rate, and (bottom) the choke-opening signals $z_{c,1}$ and $z_{c,2}$ and the implicit choke characteristic $G(t)$.

In **Fig. 6,** the measured and simulated mass-flow rates J_c are plotted compared with the measured pump-flow rate J_p. We can observe a good match between these two signals. Because the entire length of the wellbore was cased throughout this scenario, we set $J_r^l = 0$. Next, we compare the measured and simulated pressure signals at the choke and pump. In the left-hand side of **Fig. 7,** the modeled and measured choke pressures p_c are compared, where a good match is observed between the measurements and the model. The quality of this match is also an indication of the good accuracy of the implicit choke characteristic $G(t)$. Moreover, by comparing Fig. 7 with Fig. 6, which reports the flow rates, during periods when the pump flow is steady, we can observe that transients in the choke pressure p_c correspond to transients in the choke flow J_c. This is because of the compressibility of the mud, which is well-captured by the hydraulics model. The model-based and measured pump pressures $p_p = p_a(t, L)$ are plotted on the right-hand side of Fig. 7. We can clearly see a good match between these two signals. However, there are some discrepancies between the two signals as well. These discrepancies are primarily caused by imperfections in the power-law model, used for computing the friction factor. We could expect a higher accuracy by using more advanced frictional models, such as the Herschel-Bulkley model, but at the expense of additional computational complexity and one additional parameter to identify.

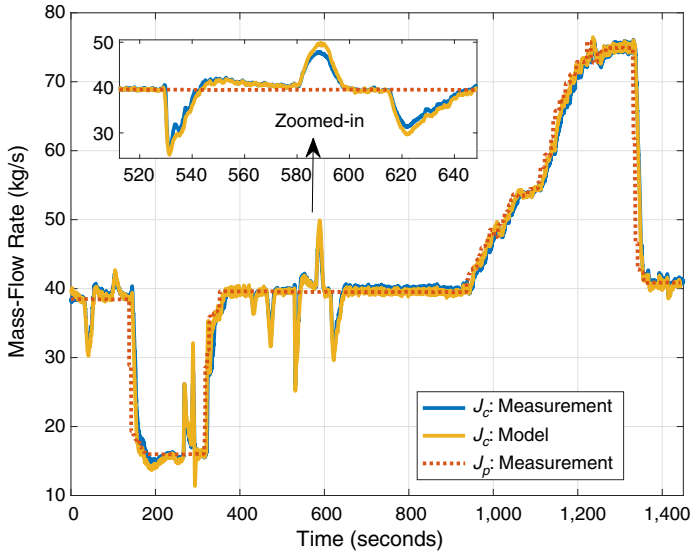

Fig. 6—Comparison of the measured and modeled choke-mass-flow rates, together with the measured pump flow.

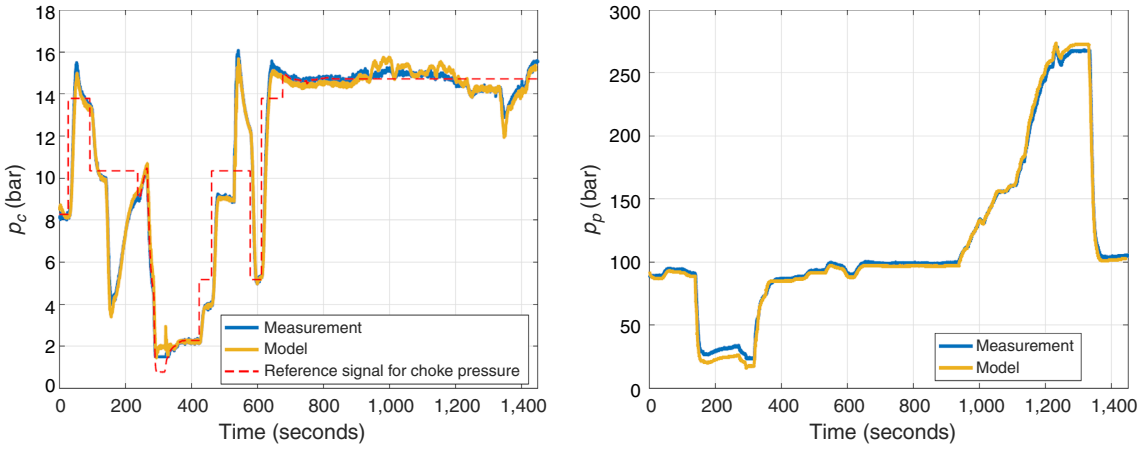

Fig. 7—Comparison of (left) the measured and modeled choke pressures, together with the reference for the choke pressure as the reference for the MPD pressure-control system, and (right) the measured and modeled pump pressures.

A careful observation of the pump- and choke-pressure measurements reveals that there is a delay of approximately 4 seconds between transients in the pump pressure and those in the choke pressure, which is exactly because pressure waves propagate at the limited speed of sound velocity. These delays are well-captured by the model, which is another indication of the high predictive capability of the hydraulics model in terms of capturing fast transients and wave-propagation effects. Moreover, in Fig. 7, the high accuracy of the surface pressure-control system of MPD can be well-observed when comparing the measured choke pressure with its reference.

Simulation Studies. The geometries of the drillstring and the annulus considered in the simulations are reported in **Fig. 8,** and the parameters are listed in **Table 2.** In this subsection, we attempt to convey the importance of having a simulation model for which the complexity is kept relatively low by including pressure-control-relevant aspects of an MPD system. We achieve this by demonstrating through simulations that theoretical analyses derived from simple design models and simulation studies are not always sufficient for obtaining a comprehensive and reliable assessment of an MPD pressure-control system, and further types of assessments (such as

semianalytic assessments) derived from a simulation model might be needed. This type of assessment might itself become impossible if the simulation model includes irrelevant or less-relevant aspects that can cause excessive complexity. However, these types of assessments are beyond the scope of this paper.

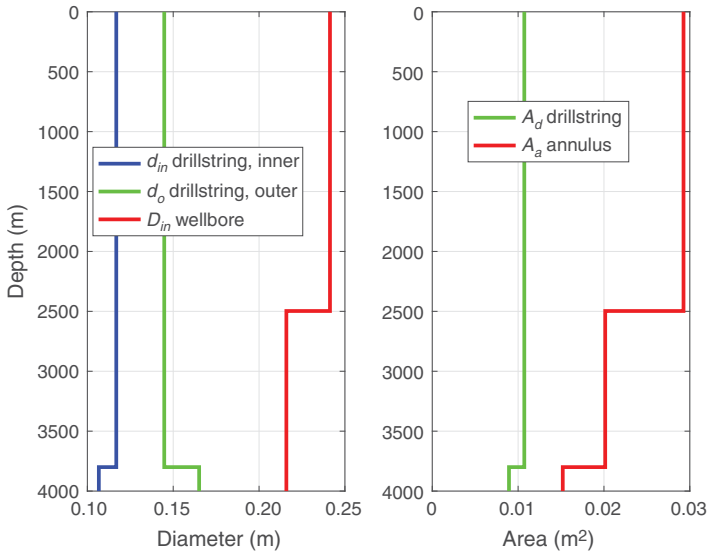

Fig. 8—Diameter and cross-sectional area of the annulus and of the drillstring considered for the simulation case studies.

Parameter	Symbol	Value	Unit
Length of the well	L	4000	m
Well inclination	$\theta(x)$	$\pi/2$	rad
Liquid-bulk modulus	β_l	1.1×10^9	Pa
Sound speed in gas	c_g	316	m/s
Reference pressure	p_0	10^5	Pa
Liquid density at p_0	ρ_0	1500	kg/m^3
Number of chokes	n_c	1	–
Choke-flow factor	$k_{c,1}$	0.0025	m^2
Average velocity	V_d	0.5	m/s
Liquid viscosity	μ_l	0.04	Pa·s
Gas viscosity	μ_g	5×10^{-6}	Pa·s
Liquid-behavior index	n_l	0.95	-
Bit-nozzle area	A_n	5.77×10^{-4}	m^2
Space-discretization-step length	Δx	12.5	m
Bit-control-volume length	Δl	$1.5\Delta x$	m
Gas-production index	κ_g	8×10^{-7}	kg/(Pa·s)
Bit-discharge coefficient	c_d	0.8	–
Profile parameter	C_0	1.1	–
Number of discretization cells	N	320	–
CFL number	CFL	0.9	–
Discretization parameter	m	20	–

Table 2—Simulation parameter values.

To compute the numerical flux functions $F_a(\cdot,\cdot)$ in Eq. 27 for the DFM of the annulus, a second-order flux-vector-splitting scheme is used (Evje and Fjelde 2002). For the drillstring, a first-order upwind scheme (LeVeque 2002) is used to compute $F_d(\cdot,\cdot)$ for Eq. 15. To obtain a simpler numerical implementation and without losing much accuracy, we linearized the flux function $f_d(\cdot)$ in Eq. 15. After this linearization, which is obtained by considering $c_l \gg v(x)$, for all $x \in (0, L)$, the flux function in Eq. 15 reduces to $f_d^T(q_d) = [\rho v, c_l^2 \rho]$, which is now linear in terms of q_d. The maximum value that the timestep Δt can take is determined by the CFL (Courant et al. 1967) condition, which is a necessary condition for the convergence of a numerical solution, as in Eq. 27. To compute the timestep, we use the relation

$$\Delta t = CFL\Delta x\overline{\lambda}, \quad \overline{\lambda} = \max\{|\lambda_{a,1}|, |\lambda_{a,2}|, |\lambda_{a,3}|, |\lambda_{d,1}|, |\lambda_{d,2}|\}, \quad (45)$$

where *CFL* is called the CFL number that should be less than unity (Courant et al. 1967). Note that while one can choose different timesteps for the drillstring and the annulus in computing Eq. 27, here we choose both to be equal and assume that $\overline{\lambda} = c_l$. For the case when there is gas in the annulus, the timestep (Eq. 45) can be highly conservative (in the sense that it is chosen much smaller than the maximum value it can take) for computing Eq. 27 for the annulus, causing a diffusive solution for the annulus. This is because even for small values of α_g in a cell, the sound velocity in that cell can drop substantially.

We perform the simulations for the following three common and representative drilling scenarios:

- For the first case study, we run the implemented model for a choke-plugging scenario; that is, a contingency where the choke effective area drops because of, for example, partial or complete blockage of the orifice by drilling cuttings. Here, we replicate such a scenario by a sudden decrease in the choke-flow factor $k_{c,1}$ in Eq. 22 during drilling ahead.
- Making a pipe connection is a common, normal drilling operation that takes place approximately every 2 to 10 hours, depending on the rate of penetration. A pipe-connection operation entails halting drilling by slowly ramping down the pump flow to zero, and then bleeding off the trapped pressure inside the drillstring by opening a bleedoff valve. Afterward, the topdrive is detached from the drillstring, and a new stand of drillpipe is screwed onto the drillstring. After that, the rig-pump flow is ramped up again, resuming the drilling.
- Gas influx, or gas kick, and subsequent gas migration in the annulus is the third scenario that will be studied. A kick usually happens when the reservoir pressure exceeds the well pressure, which can occur for reasons such as drilling into a high-pressure zone, a pressure drop during a pipe connection, or swab and surge effects. We simulate such a scenario by increasing the reservoir pressure to replicate running into an unexpected high-pressure zone.

Regarding the control system, a simple pressure-control system is used to maintain the downhole pressure during these scenarios. We design this control system using the simple lumped-parameters model in Kaasa et al. (2012). This model consists of three ordinary-differential equations, and in this model the wave-propagations effect is compromised in exchange for simplicity. Although this model is derived from a single-phase-flow assumption, it partially accounts for two-phase scenarios through the parameters related to the bulk moduli. A comparison between this design model and the simulation model is provided in **Table 3.**

Model Condition	Simulation Model	Design Model
Complexity	5 PDEs + 5 closure laws	3 ODEs
Number of dimensions	1D	1D
Number of phases	2	1
Captures liquid/liquid flows	Yes	No
Captures gas/liquid flows	Yes	No
Captures flow compressibility	Yes	No
Captures wave propagation	Yes	No
Captures gas migration	Yes	No
Captures liquid influx	Yes	Yes
Captures gas influx	Yes	No
Captures flow-pattern transitions	Yes	No
Captures variation in cross-sectional area	Yes	No
Isothermal-condition assumption	Yes	Yes
Radially homogeneous flow assumption	Yes	Yes
Axial flow assumption	Yes	Yes

Table 3—Conditions of the simulation model vs. the design model. ODE = ordinary-differential equation.

Remark 9. The focus of this paper is not on controller design, and the used controller does not necessarily provide a satisfactory pressure-control performance. The focus is rather on assessing how certain model/system aspects, taken into account in the proposed model, affect closed-loop-system performance.

Following the work by Kaasa et al. (2012), this control system is made up of two parts: a proportional-integral controller that regulates the surface pressure p_c through the choke opening z_c as the control input, and an estimator that generates a reference for the controller from the surface and downhole measurements and also the reference given for the downhole pressure p_{dh}^*. The reference generator consists of a parametrized model, approximating the surface pressure depending on a given reference for the downhole pressure, and an estimator that generates an estimate for the parameters of this model. This estimator is designed with a recursive-least-square method with a forgetting factor (Nelles 2001). Assuming laminar flow, the parametrized model is given by

$$p_c^*(t) = p_{dh}^*(t) - [J_c(t) - J_{bpp}(t)][1-\theta_f(t)]F - [1-\theta_g(t)]G, \quad \text{(46)}$$

where $F = \int_0^l \frac{32\mu_l\rho_0}{A_a(x)\overline{d}_a^2(x)}dx$ and $G = g\int_0^l \rho_0 \sin[\theta_a(x)]dx$, $\theta_f(t)$ and $\theta_g(t)$ are the to-be-estimated parameters, the estimates of which are indicated by $\hat{\theta}_f(t)$ and $\hat{\theta}_g(t)$, respectively. Here, we assume that the surface measurements are available at a high sampling rate while the downhole measurements are performed at a low rate, which is often the case in realistic drilling scenarios. Here, we take the downhole sampling period during normal operations to be $\Delta t_e = 20$ seconds. In practice, and especially in the case of long wells, there is also some delay in transmitting the downhole measurements to the surface because of the use of mud-pulse telemetry. However, we here assume that the downhole data are immediately available after measurement. Moreover, we assume that the only choke, described

by Eq. 22, has a linear characteristic in its operating range [i.e., $G_1(z_{c,1}) = z_{c,1}$ for $0 \le z_{c,1} \le 1$, and $G_1(z_{c,1}) = 0$ and $G_1(z_{c,1}) = 1$ for $z_{c,1} < 0$ and $z_{c,1} > 1$, respectively]. However, one can consider more complex characteristics for the choke through $G(\cdot)$.

Results for a Choke-Plugging Scenario. Here, the results for a choke-plugging scenario are shown. In this scenario, the choke-flow factor $k_{c,1}$ drops by 50% from its nominal value at $t = 400$ seconds. Because a laminar flow has weaker damping effects on propagating pressure waves and an objective of this subsection is to illustrate the distributed aspects of the model, we consider a laminar flow with $n_l = 1$ along the entire flow path in this scenario. The corresponding results are reported in **Fig. 9,** on the left-hand side of which are the pressure signals for both the design model and the simulation model, and on the right-hand side of which are snapshots of the liquid velocity along the flow path. As seen from the left-hand side of Fig. 9, the overall closed-loop responses in both models are similar; the design and simulation models show close dynamical behaviors in this scenario. The difference between the two models in terms of the steady-state values of the pressures p_c and p_p is because the compressibility of the liquid is not captured in the design model.

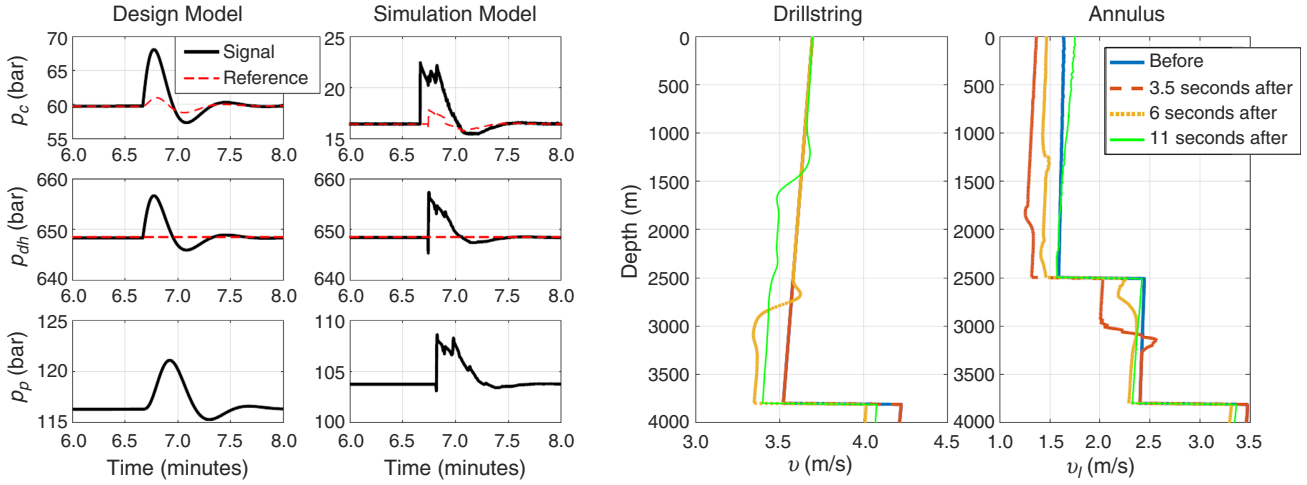

Fig. 9—Simulation results for a choke-plugging event: (left) the choke, downhole, and pump-pressure signals while comparing the design model with the simulation model; (right) snapshots of the spatial velocity profile for the simulation model before and after the event.

The developed simulation model in this paper captures the wave-propagations effects to a large extent, and these effects can be clearly observed in the left-hand side of Fig. 9 (for the simulation model) in the time delays that exist between the time when the pressure wave is generated at the surface and the times when it affects the downhole and pump pressures. In addition, the jagged behavior observed in the pressure signals is caused by the wave-propagation effects. A more insightful illustration of this effect is given in the figure in the right-hand side of Fig. 9 by the snapshots of the liquid velocity along the flow path at a variety of time instances. In particular, Fig. 9, right-hand side, illustrates the propagation and reflection of pressure waves when striking obstacles (such as the bit), as well as geometrical changes in the flow path. As can be seen, right before the choke gets plugged, the system is experiencing a nearly steady-state condition. When the choke is plugged at $t = 400$ seconds, it causes some fluctuations in the velocity (and also pressure) profiles of the system that keep propagating along the system afterward, until those are mitigated on a longer time scale, because of frictional effects and control suppression, as well as numerical dissipations.

In summary, these results show the value of the proposed model in the scope of the performance evaluation of MPD control systems.

Results for a Pipe-Connection Scenario. Next, we present the simulation results in a pipe-connection scenario. The results are presented for two sets of control parameters to further illustrate how neglecting the fast transients (such as wave-propagation effects resulting from the distributed nature of the system) in the design model can deteriorate the closed-loop performance.

In this scenario, the mass-flow rates of the mud pump and the backpressure pump change as in **Fig. 10.** When the pump-flow rate reaches a level less than one-half of its nominal value, we stop sampling the downhole variables and updating the estimator to replicate a realistic connection scenario during which the downhole measurements are not available because of the lack of mud circulation.

We first implement this scenario by considering the set of control parameters, referred to as Parameter Set 1, which are designed to lead to slow and gentle control signals and a rather slow closed-loop system in terms of recovering from disturbances such as changes in the pump flow. We report the results of these simulations in **Figs. 11 and 12.** We apply the controller to both the design model and simulation model. It is observed from Fig. 11 that the simulation model exhibits a transient behavior that is similar to that of the design model. This observation indicates that the simulation model reduces to the design model when the operations are performed slowly, such as in pipe connections. We have also shown the flow and pressure drop of the bit in Fig. 12. As expected, when the pressure drop is negative [i.e., $p_d(t, L) - p_a(t, 0) < 0$], the flow through the bit (J_{bit}) becomes zero because of the non-return valve.

Results of these simulations can, however, be misleading because they might lead one to conclude that the distributed nature of a drilling system with MPD need not be taken into account while designing a pressure controller. To show that this can be a wrong conclusion and to further highlight the considerable effects of the distributed nature the system on the closed-loop performance, we repeat the same simulation scenario, but with the second set of control parameters, referred to as Parameter Set 2, which should lead to faster control signals and better closed-loop performance in terms of recovering from disturbances. The results are plotted in **Fig. 13.** As expected, the closed-loop performance with the design model as the plant has improved. However, the response quality when this controller is applied to the simulation model has degraded unexpectedly. This has the following important implications:

- The simulation model is more realistic than the design model, and it provides a more accurate prediction of the flow and pressure behavior in a drilling system.
- One should not rely only on the theoretical results derived from the design model and the simulations on a high-fidelity simulation model because those might show perfect performance in some scenarios and poor performance in other scenarios. This can be because this controller with Parameter Set 2 results in closed-loop dynamics that are too fast that the fast dynamical aspects of the drilling system (such as the pressure wave-propagation effects) are no longer negligible.
- By having the time scale of the fast dynamics of the system, we can already predict intuitively which proportional-integral control parameters can result in poor performance without needing to perform time-consuming simulations on the simulation model. However, doing so might be challenging or even impossible when the control system is more complicated.

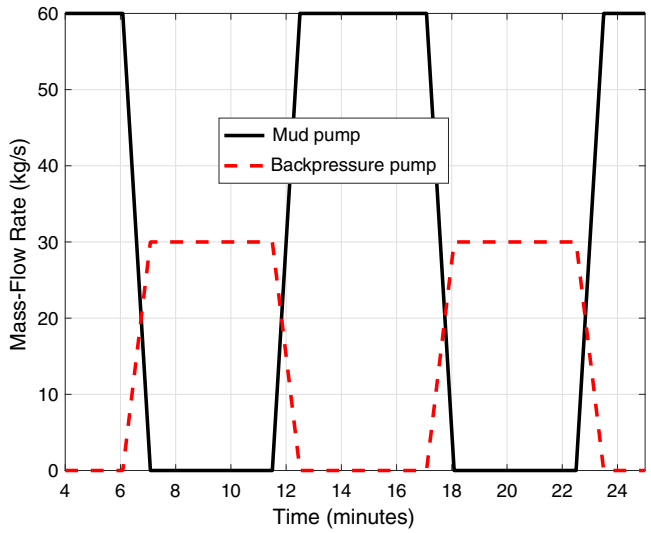

Fig. 10—Mass-flow rates of the mud pump and the backpressure pump in the connection scenario.

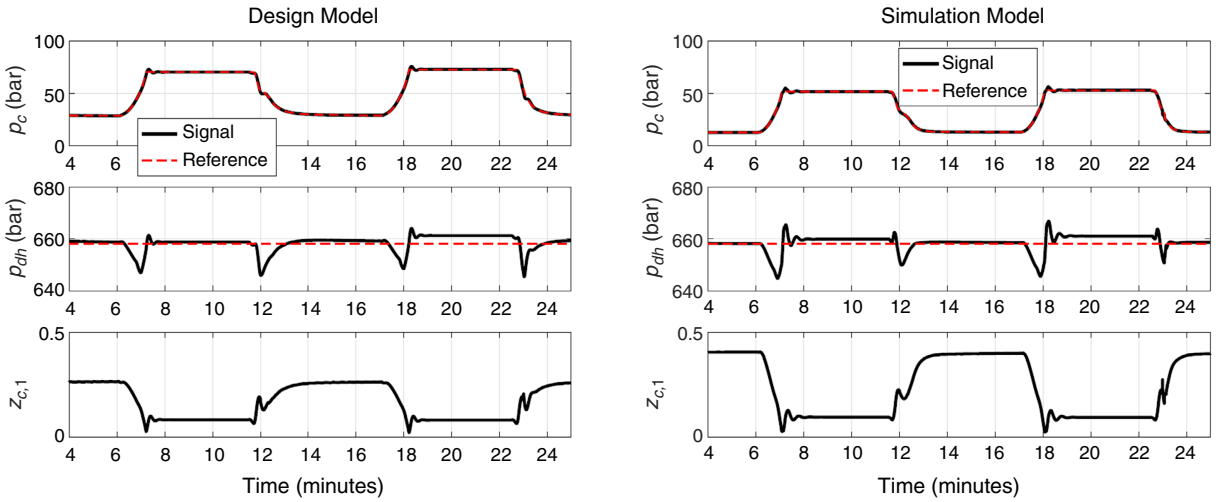

Fig. 11—Simulation results for a pipe-connection scenario for Parameter Set 1: the choke, downhole, and pump-pressure signals from (left) the design model and (right) the simulation model.

In such cases, one approach to determine the performance of the closed-loop system can be performing semianalytical system analyses together with simulation studies on the simulation hydraulics model, which includes only the pressure control aspects of MPD to allow for fast analyses and also simulations.

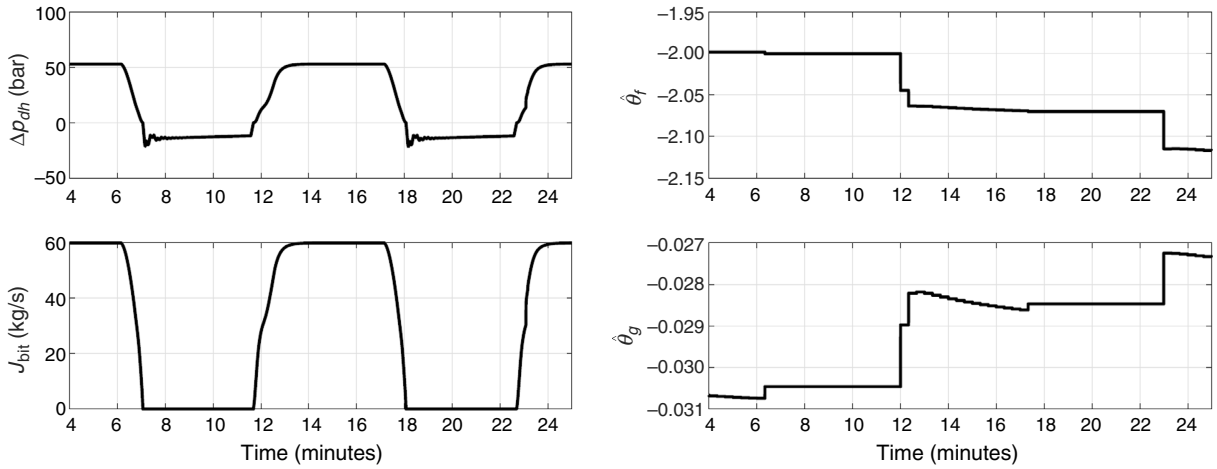

Fig. 12—Simulation results for a pipe-connection scenario for Parameter Set 1: (left) the pressure drop over the bit and the flow through it and (right) the adaptive parameters of the estimator.

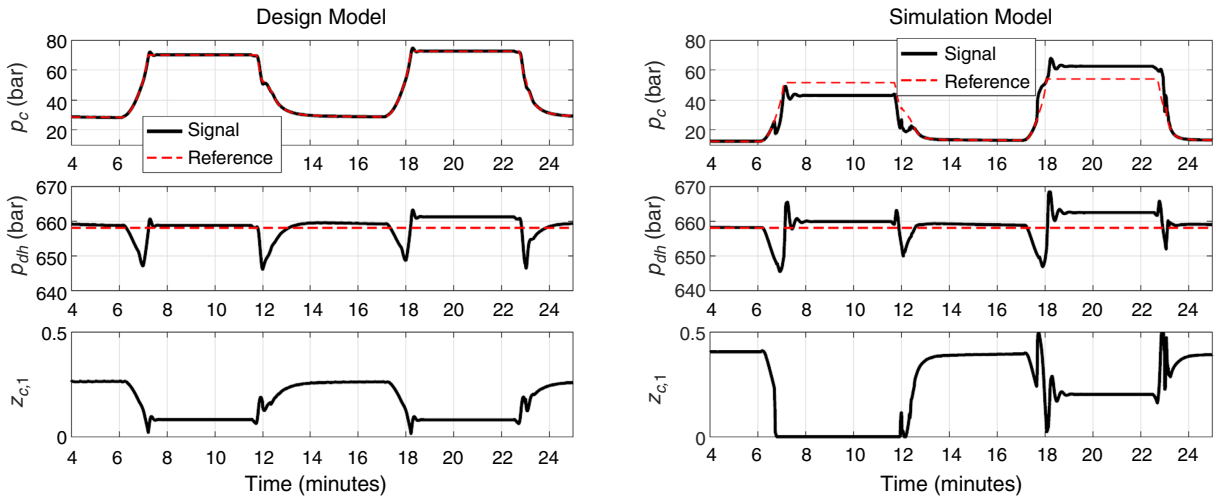

Fig. 13—Simulation results for a pipe-connection scenario for Parameter Set 2: the choke, downhole, and pump-pressure signals from (left) the design model and (right) the simulation model.

Results for a Gas-Influx Scenario. This subsection illustrates the ability of the hydraulics model to capture gas influx and migration scenarios in the annulus in a closed-loop setting with MPD. Throughout this scenario the pump-flow rate is kept constant at $J_p = 60$ kg/s. A rapid 4% increase in the reservoir pressure p_r is applied at $t = 400$ seconds, resembling the scenario of encountering a high-pressure zone while drilling. Before this time, the flow is single phase all along the flow path. Here, we assume that we can detect the resulting gas kick and also identify the new reservoir pressure some time after it begins. Afterward, a new reference, larger than the reservoir pressure, is set for the downhole pressure to prevent additional gas influxes into the wellbore. To prevent a potential control failure, this operation, changing p^*_{dh}, is performed slowly. We should mention that a common practice during a kick is to control the pump pressure rather than the downhole pressure.

The simulation results are depicted in **Figs. 14 and 15.** The choke, downhole, and pump pressures are shown on the left-hand side of Fig. 14. On the right-hand side of Fig. 14, we illustrate the choke opening together with the parameters of the estimator. We can clearly observe that when the gas reaches the surface, it leads to a rapid change in the choke opening. Moreover, the gas expansion in the annulus causes $\hat{\theta}_g$ to increase for some time, as expected, given the fact that the gas-expansion phenomenon lowers the hydrostatic pressure in the annulus. Fig. 15 gives an illustration of the gas migration and its effects on the flow rate through the choke. We can see from snapshots of the gas void fraction α_g, on the right-hand side of Fig. 15, that as the kick moves closer to the surface it expands more because of a lower pressure. The gas expansion is also illustrated in **Fig. 16.** The gas expansion also increases the mass-flow rate of the choke, as can be clearly observed from $J_c(t)$. On the contrary, when the kick reaches the surface and starts leaving the annulus through the choke, the mass-flow rate of the choke rapidly drops, starting at approximately $t = 33.5$ minutes. The steady-state difference between the accumulative mass of the influx and the accumulative mass of the gas through the choke shows that the used scheme does not exactly preserve the mass-flow rate. To obtain more accuracy in this respect, one can adapt well-balanced schemes that are more capable of preserving the steady-state response (Chertock et al. 2015). However, in general, this type of scheme is highly expensive computationally. It is observed that the control system successfully, in terms of remaining stable, circulated out the kick in this scenario. Yet it is not unreasonable to expect the failure of the designed control system in events such as a choke plugging when there is a two-phase flow in the annulus. The reason for this is large changes in the system behavior that can occur in such cases. In particular, even for small amounts of gas-void fraction α_g, the sound velocity of the flow in the annulus drops dramatically, causing the fast dynamics of the system to stop being regarded as fast. This observation again implies the importance of performing a semianalytical assessment of the performance of a pressure-control system using simulation models, in addition to simulation studies.

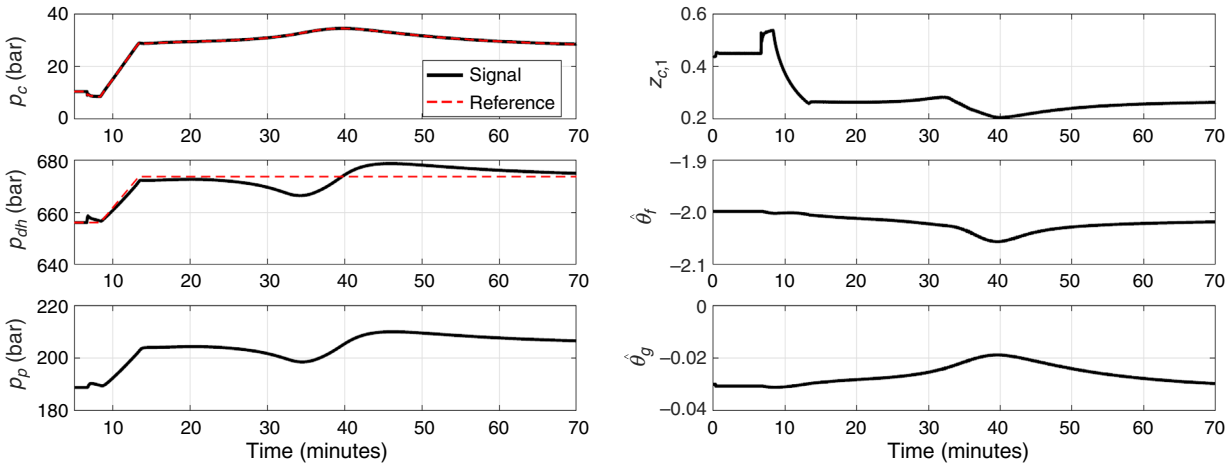

Fig. 14—Simulation results for the gas-influx scenario: (left) the choke, downhole, and pump pressures and (right) the choke opening with the adaptive parameters of the estimator.

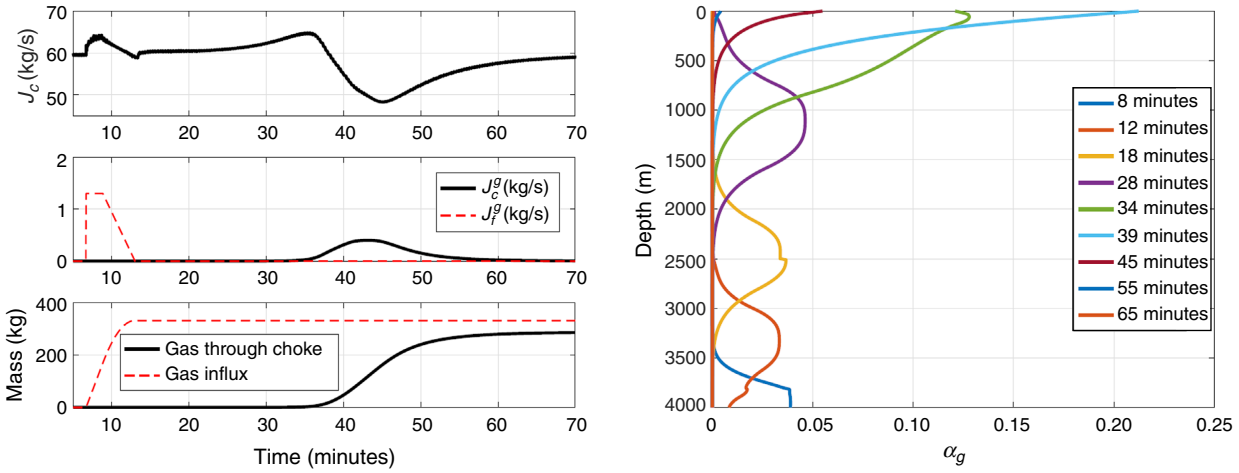

Fig. 15—Simulation results for the gas-influx scenario: (left) mixed mass-flow rate downstream the choke J_c, mass-flow rate of the gas influx J_f^g and that of the gas through the choke J_c^g, and accumulative mass of the gas influx and that of the gas through the choke, and (right) snapshots of the gas void fraction α_g along the annulus.

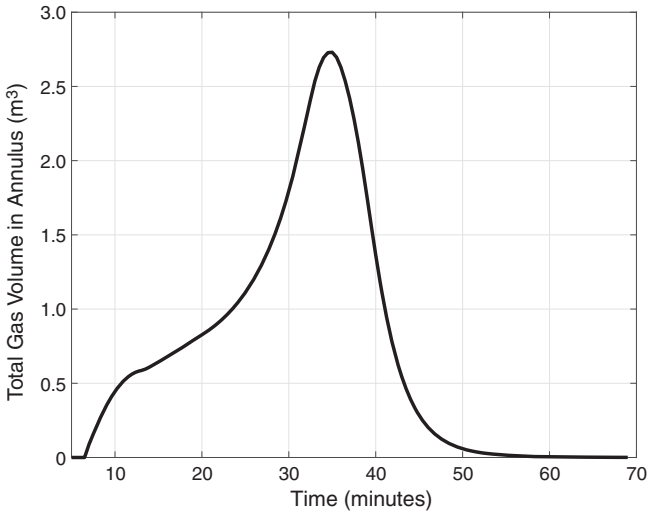

Fig. 16—Simulation results for the gas-influx scenario: the total volume of the gas in the wellbore over time.

Simulations Starting from a Transient State. In general, drilling systems with automated MPD are close to some steady-state condition for most of the drilling time. Therefore, it is reasonable to start the simulation of many drilling scenarios from a steady state of the hydraulics model. Nonetheless, a reliable MPD control system should also show robustness to situations where the system is already in a transient state when the control system takes over the control task. Therefore, in this part, we present simulation results that have been started from a transient initial condition. To design a transient initial condition for these simulations, we consider a steady state of the model without any gas in the wellbore and then add a pocket of gas to perturb it. The gas migration corresponding to this scenario is reported on the right-hand side of **Fig. 17.** In Fig. 17, the snapshot caught at the zero time shows the considered initial condition for α_g. The pump, downhole, and choke-pressure signals are reported on the left-hand side of Fig. 17. These simulations show that this hydraulics model and the numerical tool can also be used to simulate drilling scenarios starting from a transient state.

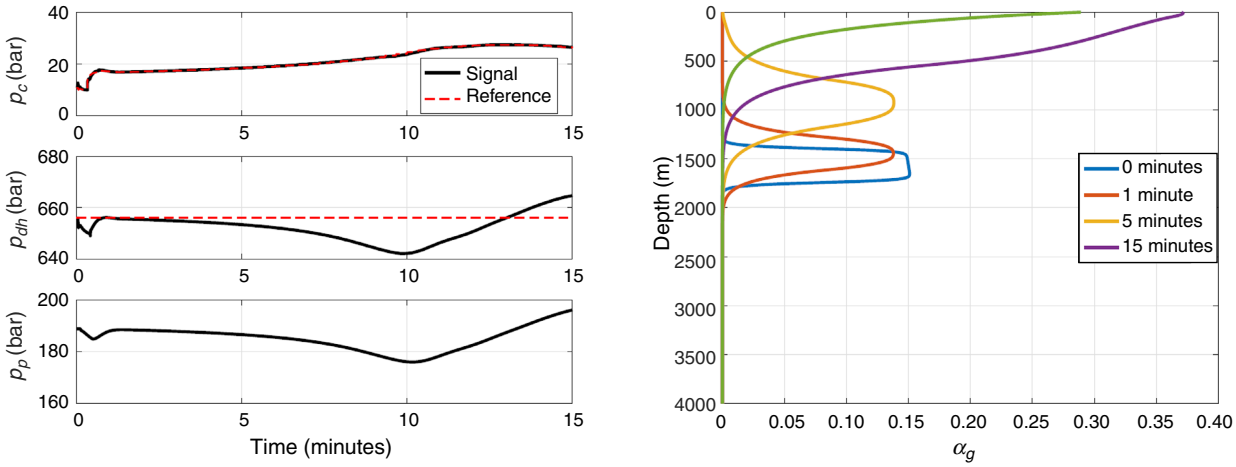

Fig. 17—Simulation results for a transient initial condition: (left) the pump, downhole, and choke-pressure signals and (right) snapshots of the gas-void fraction α_g along the annulus.

Conclusions

A two-phase hydraulics model in the form of two coupled systems of PDEs has been derived for MPD. The model complexity is limited by incorporating only the mass transport, pressure dynamics, and other aspects of an MPD system that can affect the performance of a pressure-control system in real-world drilling scenarios. Therefore, it provides a basis for evaluating the performance of pressure-control systems in virtual test scenarios. Moreover, an approach has been presented for numerical implementation of the model. Variations in the cross-sectional area of the flow path as well as the nonlinear boundary conditions are often not considered in the control design but do exist in reality, and can significantly jeopardize the performance and stability of a pressure-control system. These aspects have been captured in the model and are accounted for during numerical implementations. The predictive capability of the model and the performance of the numerical implementations have been demonstrated through illustrative case studies representing a choke-plugging, connection, and gas-influx scenario. Through these studies, we have also demonstrated the importance of keeping the complexity of an MPD simulation low. However, the developed model is not suitable for handling scenarios related to vertical motions of the drillstring, such as washing-stand and tripping scenarios. Adding this aspect to the model is the focus of ongoing research. In addition, we have illustrated the high accuracy of the model by comparing it with field data from a real-life drilling well for single-phase scenarios. A direction of our current work is the further validation of the developed MPD model in this paper by comparing simulation results and drilling field data for two-phase-flow drilling scenarios.

Nomenclature

A_a = annulus area, m^2
A_d = drillstring area, m^2
A_n = bit-nozzle area, m^2
c_d = bit-discharge coefficient
c_g = sound speed in gas, m/s
c_l = sound speed in liquid, m/s
C_0 = profile parameter
CFL = CFL number
d_{in} = inner diameter of drillstring, m
d_o = outer diameter of drillstring, m
D = hydraulic diameter, m
D_{eff} = effective diameter, m
D_{in} = wellbore diameter, m
G = choke characteristic
J_{bpp} = backpressure pump-flow rate, kg/s
J_p = rig pump-flow rate, kg/s
k_c = flow factor of choke, m^2
L = well length, m
n_c = number of choke valves
n_l = liquid-behavior index
n_m = mixture-behavior index

n = temporal discretization index
N = number of cells in discretization
p_a = pressure in annulus, Pa
p_c = choke pressure, Pa
p_d = pressure in drillstring, Pa
p_{dh} = downhole pressure, Pa
p_p = pump pressure, Pa
p_r = reservoir pressure, Pa
p_0 = reference pressure, Pa
Re = generalized Reynolds number, Pa
t = temporal variable, seconds
v = liquid velocity in drillstring, m/s
v_g = gas velocity, m/s
v_l = liquid velocity in annulus, m/s
v_m = mixture velocity, m/s
V_d = drift velocity, m/s
z_c = opening of choke
α_g = gas-void fraction
α_l = liquid-void fraction
β_g = gas-bulk modulus, Pa
β_l = liquid-bulk modulus, Pa
Δl = bit-control volume length, m
Δx = spatial discretization step size, m
Δt = discretization timestep size, seconds
ε = pipe roughness, m
θ = well inclination, rad
θ_f = frictional correction parameter
θ_g = gravitational correction parameter
$\overline{\theta}$ = average well inclination, rad
κ_g = gas-production index, kg/(Pa·s)
μ_g = gas dynamic viscosity, Pa·s
μ_l = liquid dynamic viscosity, Pa·s
μ_m = mixture viscosity, Pa·s
ν = Fanning friction factor
ρ_c = choke density, kg/m^3
ρ_g = gas density, kg/m^3
ρ_l = liquid density in annulus, kg/m^3
ρ_m = mixture density, kg/m^3
ρ_0 = liquid density at p_0, kg/m^3

Acknowledgment

This research has been performed as part of the Hydra project, which received funding from the European Union's Horizon 2020 research and innovation program (Grant No. 675731).

References

Aarsnes, U. J. F., Açıkmeşe, B., Ambrus, A. et al. 2016a. Robust Controller Design for Automated Kick Handling in Managed Pressure Drilling. *J Process Control* **47** (November): 46–57. https://doi.org/10.1016/j.jprocont.2016.09.001.

Aarsnes, U. J. F., Ambrus, A., Di Meglio, F. et al. 2016b. A Simplified Two-Phase Flow Model Using a Quasi-Equilibrium Momentum Balance. *Int J Mutiph* **83** (July): 77–85. https://doi.org/10.1016/j.ijmultiphaseflow.2016.03.017.

Aarsnes, U. J. F., Di Meglio, F., Graham, R. et al. 2016c. A Methodology for Classifying Operating Regimes in Underbalanced-Drilling Operations. *SPE J*. **21** (2): 423–433. SPE-178920-PA. https://doi.org/10.2118/178920-PA.

Aarsnes, U. J. F., Flåtten, T., and Aamo, O. M. 2016d. Review of Two-Phase Flow Models for Control and Estimation. *Annu Rev Control* **42:** 50–62. https://doi.org/10.1016/j.arcontrol.2016.06.001.

Abbasi, M. H., Naderi Lordejani, S., Velmurugan, N. et al. 2019. A Godunov-Type Scheme for the Drift Flux Model with Variable Cross Section. *J Pet Sci Eng* **179** (August): 796–813. https://doi.org/10.1016/j.petrol.2019.04.089.

Ambrus, A., Aarsnes, U. J. F., Karimi Vajargah, A. et al. 2016. Real-Time Estimation of Reservoir Influx Rate and Pore Pressure Using a Simplified Transient Two-Phase Flow Model. *J Nat Gas Sci Eng* **32** (May): 439–452. https://doi.org/10.1016/j.jngse.2016.04.036.

Berg, C., Evjen, G. A., Velmurugan, N. et al. 2019a. The Influx-Management Envelope Considering Real-Fluid Behavior. *SPE Drill & Compl* SPE-198916-PA (in press; posted December 2019). https://doi.org/10.2118/198916-PA.

Berg, C., Stakvik, J. Å., Lie, B. et al. 2019b. Pressure Wave Propagation in Managed Pressure Drilling—Model Comparison with Real Life Data. *Proc.,* 60th SIMS Conference on Simulation and Modelling, Västerås, Sweden, 12–16 August, 91–98. https://doi.org/10.3384/ecp2017091.

Bhagwat, S. M. and Ghajar, A. J. 2014. A Flow Pattern Independent Drift Flux Model Based Void Fraction Correlation for a Wide Range of Gas-Liquid Two Phase Flow. *Int J Multiph* **59** (February): 186–205. https://doi.org/10.1016/j.ijmultiphaseflow.2013.11.001.

Cayeux, E., Daireaux, B., Dvergsnes, E. et al. 2012. Advanced Drilling Simulation Environment for Testing New Drilling Automation Techniques and Practices. *SPE Drill & Compl* **27** (4): 559–573. SPE-150941-PA. https://doi.org/10.2118/150941-PA.

Chertock, A., Cui, S., Kurganov, A. et al. 2015. Well-Balanced Positivity Preserving Central-Upwind Scheme for the Shallow Water System with Friction Terms. *Int J Numer Methods Fluids* **78** (6): 355–383. https://doi.org/10.1002/fld.4023.

Cook, C., Balachandar, S., Chung, J. et al. 2018. A Generalized Characteristic-Based Split Projection Method for Navier-Stokes with Real Fluids. *Int J Heat Mass Transf* **124** (September): 1045–1058. https://doi.org/10.1016/j.ijheatmasstransfer.2018.03.054.

Courant, R., Friedrichs, K., and Lewy, H. 1967. On the Partial Difference Equations of Mathematical Physics. *IBM J Res Dev* **11** (2): 215–234. https://doi.org/10.1147/rd.112.0215.

de Carvalho, M. A. D., de Moraes Oliveira, G. F., Fernandes, L. D. et al. 2019. Two-Phase Flow Model Validation During Conventional/Pressurized Mud Cap Drilling (PCMD) Scenarios. *J Pet Sci Eng* **172** (January): 314–326. https://doi.org/10.1016/j.petrol.2018.09.037.

Di Meglio, F. 2011. *Dynamics and Control of Slugging in Oil Production*. PhD dissertation, École Nationale Supérieure des Mines de Paris, Paris, France (July 2011).

Di Meglio, F., Kaasa, G. O., and Petit, N. 2009. A First Principle Model for Multiphase Slugging Flow in Vertical Risers. *Proc.,* 48th IEEE Conference on Decision and Control (CDC) held jointly with 2009 28th Chinese Control Conference, Shanghai, China, 15–18 December, 8244–8251. https://doi.org/10.1109/CDC.2009.5400680.

Di Meglio, F., Kaasa, G. O., Petit, N. et al. 2011. Slugging in Multiphase Flow as a Mixed Initial-Boundary Value Problem for a Quasilinear Hyperbolic System. *Proc.,* 2011 American Control Conference, San Francisco, California, USA, 29 June–1 July, 3589–3596. https://doi.org/10.1109/ACC.2011.5991300.

Evje, S. and Fjelde, K. K. 2002. Hybrid Flux-Splitting Schemes for a Two-Phase Flow Model. *J Comput Phys* **175** (2): 674–701. https://doi.org/10.1006/jcph.2001.6962.

Fjelde, K. K. and Karlsen, K. H. 2002. High-Resolution Hybrid Primitive–Conservative Upwind Schemes for the Drift Flux Model. *Comput Fluids* **31** (3): 335–367. https://doi.org/10.1016/S0045-7930(01)00041-X.

Gavrilyuk, S. L. and Fabre, J. 1996. Lagrangian Coordinates for a Drift-Flux Model of a Gas-Liquid Mixture. *Int J Multiph* **22** (3): 453–460. https://doi.org/10.1016/0301-9322(95)00085-2.

Godhavn, J.-M. 2010. Control Requirements for Automatic Managed Pressure Drilling System. *SPE Drill & Compl* **25** (3): 336–345. SPE-119442-PA. https://doi.org/10.2118/119442-PA.

Godhavn, J.-M., Pavlov, A., Kaasa, G.-O. et al. 2011. Drilling Seeking Automatic Control Solutions. *IFAC Proc Volumes* **44** (1): 10842–10850. https://doi.org/10.3182/20110828-6-IT-1002.00551.

Ishii, M. and Hibiki, T. 2011. *Thermo-Fluid Dynamics of Two-Phase Flow*. New York, New York, USA: Springer.

Kaasa, G.-O., Stamnes, Y. N., Aamo, O. M. et al. 2012. Simplified Hydraulics Model Used for Intelligent Estimation of Downhole Pressure for a Managed-Pressure-Drilling Control System. *SPE Drill & Compl* **27** (1): 127–138. SPE-143097-PA. https://doi.org/10.2118/143097-PA.

Kröner, D. and Thanh, M. D. 2005. Numerical Solutions to Compressible Flows in a Nozzle with Variable Cross-Section. *SIAM J Numer Anal* **43** (2): 796–824. https://doi.org/10.1137/040607460.

Lage, A. C. V. M., Fjelde, K. K., and Time, R. W. 2003. Underbalanced Drilling Dynamics: Two-Phase Flow Modeling and Experiments. *SPE J*. **8** (1): 61–70. SPE-83607-PA. https://doi.org/10.2118/83607-PA.

Landet, I. S., Mahdianfar, H., Aarsnes, U. J. F. et al. 2012. Modeling for MPD Operations with Experimental Validation. Paper presented at the IADC/SPE Drilling Conference and Exhibition, San Diego, California, USA, 6–8 March. SPE-150461-MS. https://doi.org/10.2118/150461-MS.

Landet, I. S., Pavlov, A., and Aamo, O. M. 2013. Modeling and Control of Heave-Induced Pressure Fluctuations in Managed Pressure Drilling. *IEEE Trans Control Syst Technol* **21** (4): 1340–1351. https://doi.org/10.1109/TCST.2012.2204751.

LeVeque, R. J. 2002. *Finite Volume Methods for Hyperbolic Problems*. Cambridge, UK: Cambridge University Press.

Livescu, S. 2012. Mathematical Modeling of Thixotropic Drilling Mud and Crude Oil Flow in Wells and Pipelines—A Review. *J Pet Sci Eng* **98–99** (November): 174–184. https://doi.org/10.1016/j.petrol.2012.04.026.

Naderi Lordejani, S., Besselink, B., Abbasi, M. H. et al. 2018. Model Order Reduction for Managed Pressure Drilling Systems Based on a Model with Local Nonlinearities. *IFAC-PapersOnLine* **51** (8): 50–55. https://doi.org/10.1016/j.ifacol.2018.06.354.

Nelles, O. 2001. *Nonlinear System Identification: From Classical Approaches to Neural Networks and Fuzzy Models*. Berlin, Germany: Springer-Verlag.

Nikoofard, A., Aarsnes, U. J. F., Johansen, T. A. et al. 2017. State and Parameter Estimation of a Drift-Flux Model for Underbalanced Drilling Operations. *IEEE Trans Control Syst Technol* **25** (6): 2000–2009. https://doi.org/10.1109/TCST.2016.2638683.

Nygaard, G. and Nævdal, G. 2006. Nonlinear Model Predictive Control Scheme for Stabilizing Annulus Pressure During Oil Well Drilling. *J Process Control* **16** (7): 719–732. https://doi.org/10.1016/j.jprocont.2006.01.002.

Pedersen, T., Aarsnes, U. J. F., and Godhavn, J.-M. 2018. Flow and Pressure Control of Underbalanced Drilling Operations Using NMPC. *J Process Control* **68** (August): 73–85. https://doi.org/10.1016/j.jprocont.2018.05.001.

Pedersen, T., Godhavn, J.-M., and Schubert, J. 2015. Supervisory Control for Underbalanced Drilling Operations. *IFAC-PapersOnLine* **48** (6): 120–127. https://doi.org/10.1016/j.ifacol.2015.08.019.

Prebeg, M., Flåtten, T., and Müller, B. 2015. Boundary and Source Term Treatment in the Large Time Step Method for a Common Two-Fluid Model. Oral presentation given at the 11th International Conference on CFD in the Minerals and Process Industries, CSIRO, Melbourne, Australia, 7–9 December.

Prebeg, M., Flåtten, T., and Müller, B. 2017. Large Time Step Roe Scheme for a Common 1D Two-Fluid Model. *Appl Math Model* **44** (April): 124–142. https://doi.org/10.1016/j.apm.2016.12.010.

Reed, T. D. and Pilehvari, A. A. 1993. A New Model for Laminar, Transitional, and Turbulent Flow of Drilling Muds. Paper presented at the SPE Production Operations Symposium, Oklahoma City, Oklahoma, USA, 21–23 March. SPE-25456-MS. https://doi.org/10.2118/25456-MS.

Rommetveit, R. and Vefring, E. H. 1991. Comparison of Results from an Advanced Gas Kick Simulator with Surface and Downhole Data from Full Scale Gas Kick Experiments in an Inclined Well. Paper presented at the SPE Annual Technical Conference and Exhibition, Dallas, Texas, USA, 6–9 October. SPE-22558-MS. https://doi.org/10.2118/22558-MS.

Shekari, Y., Hajidavalloo, E., and Behbahani-Nejad, M. 2013. Reduced Order Modeling of Transient Two-Phase Flows and Its Application to Upward Two-Phase Flows in the Under-Balanced Drilling. *Appl Math Comput* **224** (1 November): 775–790. https://doi.org/10.1016/j.amc.2013.09.023.

Stamnes, Ø. N., Zhou, J., Kaasa, G. O. et al. 2008. Adaptive Observer Design for the Bottomhole Pressure of a Managed Pressure Drilling System. Paper presented at the 2008 47th IEEE Conference on Decision and Control, Cancun, Mexico, 9–11 December, 2961–2966. https://doi.org/10.1109/CDC.2008.4738845.

Strecker, T., Aamo, O. M., and Manum, H. 2017. Simulation of Heave-Induced Pressure Oscillations in Herschel-Bulkley Muds. *SPE J*. **22** (5): 1635–1653. SPE-185947-PA. https://doi.org/10.2118/185947-PA.

Swanee, P. and Jain, A. K. 1976. Explicit Equations for Pipe-Flow Problems. *J Hydraul Div* **102** (5): 657–664.

Sweby, P. K. 1984. High Resolution Schemes Using Flux Limiters for Hyperbolic Conservation Laws. *SIAM J Numer Anal* **21** (5): 995–1011. https://doi.org/10.1137/0721062.

Udegbunam, J. E., Fjelde, K. K., Evje, S. et al. 2015. On the Advection-Upstream-Splitting-Method Hybrid Scheme: A Simple Transient-Flow Model for Managed-Pressure-Drilling and Underbalanced-Drilling Applications. *SPE Drill & Compl* **30** (2): 98–109. SPE-168960-PA. https://doi.org/10.2118/168960-PA.

Vishnumolakala, N., Gildin, E., and Noynaert, S. 2015. A Simulation Environment for Automatic Managed Pressure Drilling Control. *IFAC-PapersOnLine* **48** (6): 128–133. https://doi.org/10.1016/j.ifacol.2015.08.020.

Wei, N., Xu, C., Meng, Y. et al. 2018. Numerical Simulation of Gas-Liquid Two-Phase Flow in Wellbore Based on Drift Flux Model. *Appl Math Comput* **338** (1 December): 175–191. https://doi.org/10.1016/j.amc.2018.03.067.

Appendix A—Approximate Solution for Turbulent Flows

We here present an approximate solution to Eq. 6 using a first-order Taylor-series expansion. From Eq. 6, we define

$$H(\nu) := \frac{1}{\sqrt{\nu}} + 4\log\left\{\frac{0.27\varepsilon}{D_{\text{eff}}} + \frac{1.26^{n_m^{-1.2}}}{\left[\nu^{(1-\frac{n_m}{2})}\text{Re}\right]^{n_m^{-0.75}}}\right\}, \quad \text{(A-1)}$$

such that $H(\nu) = 0$. We take

$$\nu = \nu_0 - \Delta\nu, \quad \text{(A-2)}$$

where

$$\nu_0 = \frac{1}{16\left[\log\left(\frac{0.27\varepsilon}{D_{\text{eff}}} + \frac{5.74}{\text{Re}^{0.9}}\right)\right]^2}, \quad \text{(A-3)}$$

is a well-known approximate solution to the Colebrook equation, which is recovered from Eq. A-1 for $n_m = 1$ (Swanee and Jain 1976). Moreover, $\Delta\nu$ is a parameter that is to be approximated. Now, using a Taylor expansion of $H(\nu)$ around ν_0, we obtain

$$H(\nu) \approx H(\nu_0) - H'(\nu_0)\Delta\nu, \quad \text{(A-4)}$$

where $H'(\nu_0) = \frac{dH}{d\nu}(\nu_0)$ is available analytically. Following Eq. A-4, designing $\Delta\nu$ as

$$\Delta\nu = \frac{H(\nu_0)}{H'(\nu_0)}, \quad \text{(A-5)}$$

leads to $H(\nu_0 - \Delta\nu) \approx 0$. Substituting this design of $\Delta\nu$ into Eq. A-2 further leads to an explicit approximation for the friction factor,

$$\nu \approx \nu_0 - \frac{H(\nu_0)}{H'(\nu_0)}. \quad \text{(A-6)}$$

One can expand Eq. A-6 to obtain a closed-form description of it to reduce the computational burden during simulations. Our numerical evaluations verified the high accuracy of this approximate solution over a wide range of Reynold's numbers and $0.6 < n_m < 1.4$.

Appendix B—Derivation of the Dynamical Bit Equation

The bit equation is obtained by considering a control volume filled with only liquid over the bit, as illustrated in Fig. 3, and averaging the momentum-conservation equation for liquid over the control volume. For the first and second halves of this control volume, each of the length $\Delta l/2$, in the drilling and annulus, we obtain, respectively,

$$\frac{\Delta l}{2}\frac{dz(t)}{dt} = A_d(L)\left[\frac{z^2(t)}{A_d(L)\rho(t,L-\Delta l/2)} - \frac{z^2(t)}{A_d(l)\rho(t,L)} + p_d(t,L-\Delta l/2) - p_d(t,L)\right] + \tilde{s}_d(t), \quad \text{(B-1)}$$

$$\frac{\Delta l}{2}\frac{dz(t)}{dt} = -A_a(0)\left[\frac{z^2(t)}{A_a(0)\rho_a(t,\Delta l/2)} - \frac{z^2(t)}{A_a(0)\rho_a(t,0)} + p_a(t,\Delta l/2) - p_a(t,0)\right] + \tilde{s}_a(t), \quad \text{(B-2)}$$

where $z(t)$ is an approximation of the average mass-flow rate in this control volume, which also gives an approximation of the flow through the bit. Note that we have also assumed a single-phase flow in the one-half of this control volume that is in the annulus. Moreover, $\tilde{s}_d = A_d(L)\int_{L-\Delta l/2}^{L} s_d(u_d,t,x)dx$ and $\tilde{s}_a = A_a(0)\int_0^{\Delta l/2} s_a(u_a,t,x)dx$. These terms can be approximated as

$$\tilde{s}_d(t) \simeq A_d(L)\frac{\Delta l}{2}s_d\left(U_{d,N},t,L-\frac{\Delta l}{2}\right), \quad \tilde{s}_a(t) \simeq A_a(0)\frac{\Delta l}{2}s_a\left(U_{a,1},t,\frac{\Delta l}{2}\right). \quad \text{(B-3)}$$

Next, considering that $\rho(t,L-\Delta l/2) \simeq \rho(t,L)$ and $\rho_a(t,\Delta l/2) \simeq \rho_a(t,0)$, subtracting Eq. B-1 from Eq. B-2 results in

$$A_a(0)p_a(t,0) + A_d(L)p_d(t,L) = A_a(0)p_a(t,\Delta l/2) + A_d(L)p_d(t,L-\Delta l/2) - \tilde{s}_d(t) + \tilde{s}_a(t). \quad \text{(B-4)}$$

Now, given the bit equation in Eq. 18, we have

$$p_d(t,L) - p_a(t,0) = \frac{1}{2\rho(t,L)}\left[\frac{z(t)}{c_d A_n}\right]^2, \quad z > 0. \quad \text{(B-5)}$$

If we solve Eqs. B-4 and B-5 for $p_d(t,L)$ and $p_a(t,0)$ and substitute the solution into the summation of Eqs. B-1 and B-2, we obtain the bit equation (Eq. 39).